NORWEGIAN JOURNAL OF GEOLOGY
https://dx.doi.org/10.1785/njg102-2-2

GEOLOGICAL SOCIETY OF NORWAY

Petrology of the crystalline crust in the southwestern Barents Sea inferred from geophysical data

Christine Fichler[1], Zeudia Pastore[1]

[1]IGP / Norwegian University of Science and Technology, S.P. Andersens veg 151, N-7031 Trondheim, Norway
E-mail corresponding author (Christine Fichler): Christine.Fichler@ntnu.no

Keywords:
- *Barents Sea*
- *Seiland Igneous Province*
- *Petrology*
- *Batholiths*
- *Ultramafic complexes*
- *Serpentinization*
- *Magnetic anomalies*
- *Gravity anomalies*
- *Geomagnetic reversal*

Received:
14. June 2021

Accepted:
8. March 2022

Published online:
5. May 2022

We present a new petrological model of the crystalline crust in the southwestern Barents Sea derived in a comprehensive workflow that focuses on the interpretation of gravity, magnetic and seismic data and that incorporates geology and petrophysics. The workflow started with the careful construction of a 3D density model of sediments, crystalline crust and upper mantle. The sedimentary model was built from published information including well logs, net erosion and salt occurrences. Existing maps of top crystalline basement and Moho depths were improved by means of deep seismic profiles. Mantle densities were derived from values of analogous geological settings. Subsequently, modelling and inversion of gravity and magnetic data resulted in densities and magnetic susceptibilities of the crystalline crust. These parameters were interpreted by comparison with published ranges of crustal rock parameters. The latter were linked to a two-dimensional colour scale dedicated to combine the mapped crustal densities and magnetic susceptibilities into a single map, a novel "crustal petrophysical attribute" map that assisted in the classification of the rock types. The eastern Bjørnøya Basin, Veslemøy High and Senja Ridge were interpreted as consisting of mafic–ultramafic crustal rocks. There is evidence for serpentinisation at the eastern Veslemøy High. It is argued that intrusions on the Veslemøy High have the same magmatic origin as the Seiland Igneous Province. The Loppa High area was interpreted to consist of upper crustal felsic–intermediate rocks of Precambrian age intruded by chains of Carboniferous intermediate–mafic intrusions. The surrounding basins and Finnmark Platform were interpreted as largely felsic–mafic metamorphic and metasedimentary rocks. A gradual change in polarity of magnetic anomalies from the Harstad Basin through the Sørvestsnaget Basin was explained by a change in direction of magnetic remanence of sills, dykes and basalts.

Introduction

The petrology of a rock provides clues about its origin and later changes through tectonic, metamorphic and magmatic processes (cf., Winter, 2010). In the subsurface, where there is no direct access to the rocks, integrated geophysical methods can capture certain properties of the petrology in the form of parameterised models. Such models are of an appreciably lower resolution than the outcrop scale and are therefore well-suited to detect and outline petrological and structural characteristics on a regional scale (cf., Dentith & Mudge, 2014).

Fichler, C. & Pastore, Z. 2022: Petrology of the crystalline crust in the southwestern Barents Sea inferred from geophysical data. Norwegian Journal of Geology 102, 202206. https://dx.doi.org/10.17850/njg102-2-2

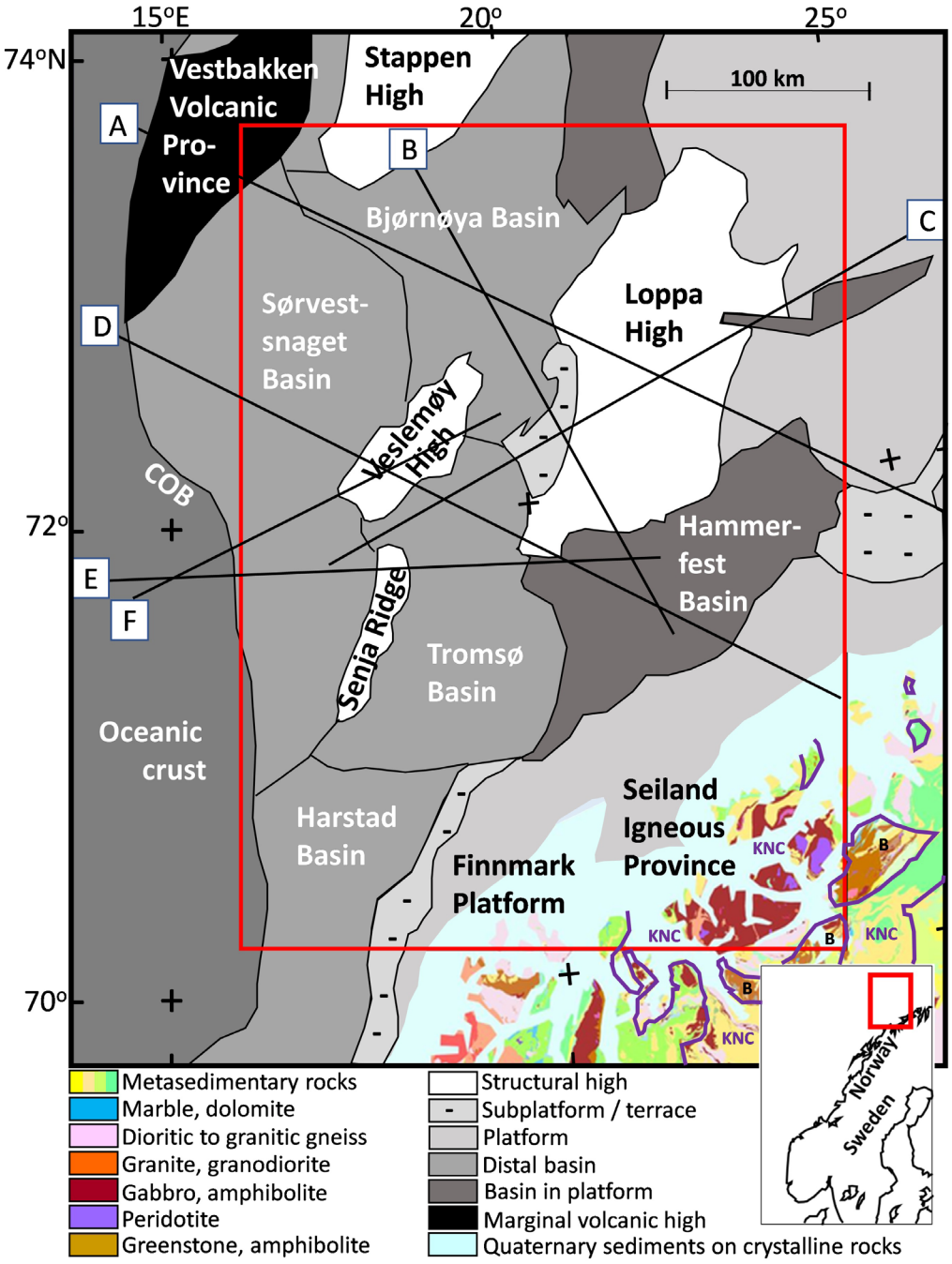

Figure 1. Offshore structural elements at base Cretaceous level (Norwegian Petroleum Directorate: www.factmaps.npd.no/factmaps/3_0/ visited 11.01.2022, based on Gabrielsen et al., 1984, 1990) and onshore geological map (Geological Survey of Norway: www.ngu.no/emne/kart-pa-nett "Berggrunn 1:250,000 vektor (Gammel)" visited 11.01.2022) with B – parautochthonous basement, KNC – Kalak Nappe Complex, (Corfu et al., 2014); superimposed are the seismic profiles: (A) – PETROBAR-07 (Clark et al., 2013), (B) – NBR07-232948 (Gernigon et al., 2014), (C) – OBS profile 1 (Aarseth, 2018), (D) – IKU-C (Ritzmann & Faleide, 2007), (E) – WBS-4/7142 (Breivik et al., 1999; Faleide et al., 2008), (F) – OBS profile A (Mjelde et al., 2002). Red box shows the location of the modelled area. Projection: UTM33, datum: WGS84.

The study area (Fig. 1), subjected to geophysical interpretation, extends from the Harstad Basin in the south to the Sørvestsnaget Basin in the north, and from the Continent-Ocean-Boundary (COB) in the west to the Norwegian mainland in the east and contains prominent crystalline basement highs with the Loppa High, Veslemøy High and Senja Ridge. The southwestern Barents Sea is at present times a passive margin (cf., Faleide et al., 2008) with characteristics of a transform margin (cf., Lundin et al., 2022). Its geological history encompasses an impressive tectonic record with opening and closure of the Iapetus Ocean, mountain building and collapse, opening of the Norwegian–Greenland Sea,

as well as multiple rifting and magmatic events (cf., Smelror et al., 2009) leading to a complex petrology in the crystalline crust studied in this paper. The term 'crust' will continue to be used in the rest of the manuscript for simplicity in the sense of 'crystalline crust'. Geophysical interpretation of the crustal petrology is a challenging task, as only a few boreholes and the adjacent Norwegian mainland provide direct evidence of crustal rock types. The geophysical interpretation utilised gravity and magnetic data, which are an expression of the distribution of the rock's densities and magnetic attributes, respectively (cf., Dentith & Mudge, 2014). Rock types have a characteristic combination of density- and magnetic attribute ranges which allows a coarse assessment of the rock type based on modelled densities and magnetic attributes. Challenges with this approach are met for rock types with highly overlapping parameter ranges, but knowledge of the geological context may allow interpretation of a more likely rock type.

The gravity and magnetic data of the study area are shown in Fig. 2. A brief look at the gravity anomalies (Fig. 2A) of the most prominent basement highs shows that the largest positive gravity anomalies are located on the offshore Senja Ridge (SR) and Veslemøy High (VH), whereas the Loppa High (LH) has only small positive gravity anomalies. On the contrary, the magnetic data (Fig. 2B) show that the Loppa High area exhibits the largest magnetic anomalies. This is a clear indication that the crustal rocks of the Loppa High differ in petrology from those of the Veslemøy High and Senja Ridge.

The large gravity anomalies of the Veslemøy High and Senja Ridge were interpreted in earlier work. Riis et al. (1986) were the first to suggest rocks of uncommonly high density (2.9 g/cm^3) in the crust of the Senja Ridge from gravity modelling along a seismic profile. From the similarity of their gravity expressions, they suggested that these high densities are also valid for the Veslemøy High. The next study was performed by Mjelde et al. (2002) along an Ocean Bottom Seismic (OBS) profile (profile F in Fig. 1) across the Veslemøy High integrating seismic interpretation with gravity and magnetic modelling. They explained the gravity high by intrusive bodies with elevated crustal densities correlating with high seismic velocities. A regional and relatively low-resolution 3D density model over the entire Barents Sea by Ebbing et al. (2007) attributed the high gravity anomalies of both Veslemøy High and Senja Ridge to lower crustal rocks with densities between 3.05 and 3.15 g/cm^3. High-density rocks were also modelled in a more detailed 3D gravity model by Barrère et al. (2011), but remarkably, only in the transition between the Loppa High and Bjørnøya Basin. Gernigon et al. (2014) modelled gravity and magnetic data along a deep seismic profile (profile B in Fig. 1) resulting in elevated densities of up to 3.1 g/cm^3 below the eastern part of the Bjørnøya Basin. In summary, the publications agree that there are high crustal densities in this part of the southwestern Barents Sea and have captured parts of these anomalous bodies. However, a more continuous map of these bodies is lacking, and their origin is a matter of debate. Both items are addressed in this work.

Previous geophysical work on the petrology of the Loppa High has consistently suggested that a lower crustal body (LCB) with high densities and high seismic velocities is present beneath the entire Loppa High, albeit with models of varying thickness and different geophysical parameters (Ritzmann & Faleide, 2007; Barrère et al., 2011; Marello et al., 2013; Clark et al., 2013; Gernigon et al., 2014; Shulgin et al., 2020). However, there are different interpretations of the high-magnetic anomalies of the Loppa high, whose origin was assigned to the upper crust (Ritzmann & Faleide, 2007; Barrère et al., 2011; Gernigon et al., 2014), while other models (Indrevær et al., 2017; Aarseth, 2018) assign these high-magnetic anomalies to the LCB. The modelling results of this publication will contribute to this discussion and add further complexity to the crust of the Loppa High.

The aim of this work was to develop a new and continuous crustal model of the southwestern Barents Sea with densities and magnetic properties using 3D modelling of gravity and magnetic field data, constrained by deep seismic profiles and well data. This model formed the basis for the subsequent interpretation of the crustal petrology guided by petrophysics and geological knowledge.

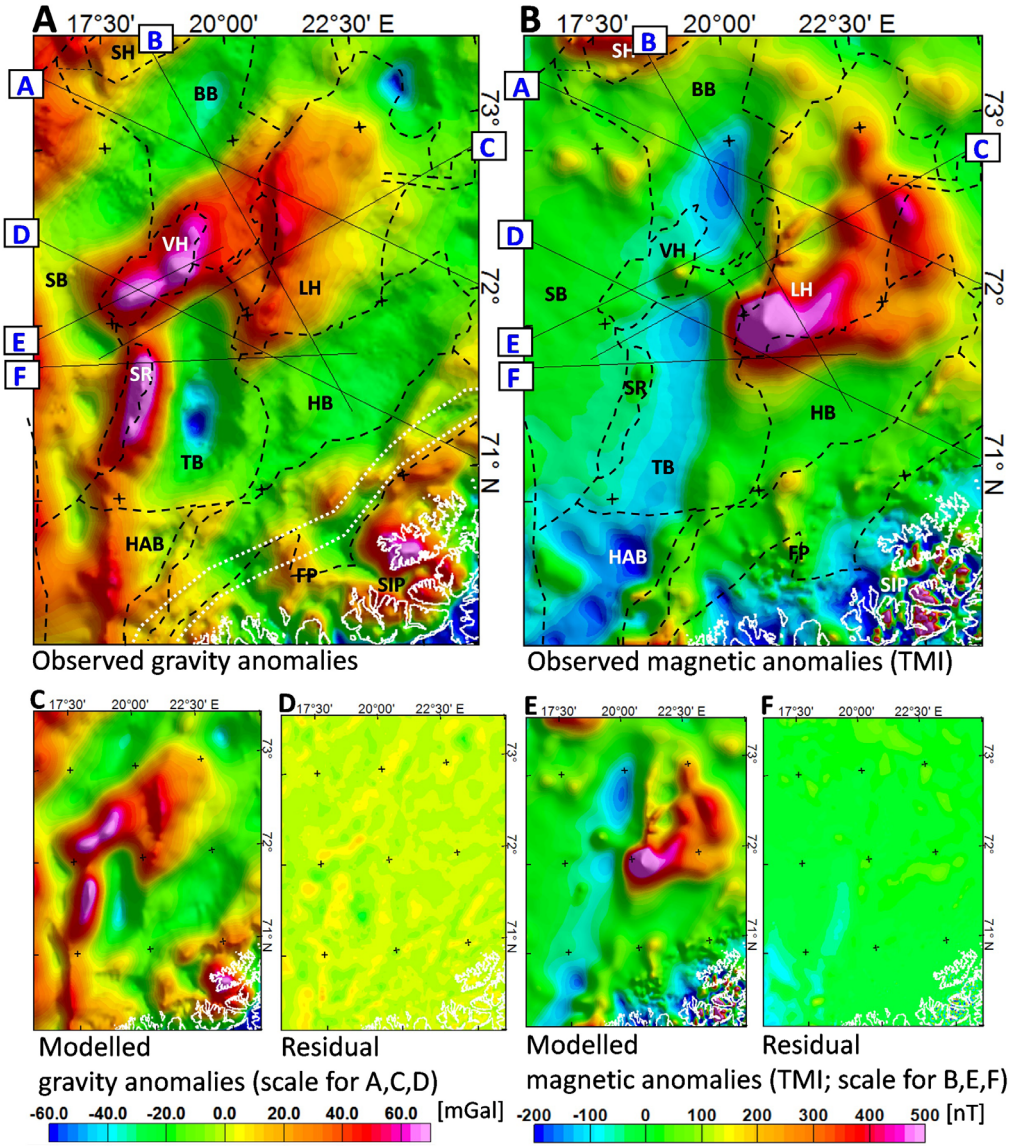

Figure 2. (A) Compilation of onshore Bouguer gravity data and offshore marine free-air gravity data (Olesen et al., 2010), the nearshore area is covered by satellite free-air gravity data (Sandwell et al., 2014) and merged with the marine free-air gravity data (Olesen et al., 2010) in the area framed by white dotted lines. (B) Magnetic anomalies (TMI – total magnetic intensity; Olesen et al., 2010); boundaries of structural elements (black dashed, details in Fig. 1); seismic profiles (black lines, details in Fig. 1). (C) Modelled gravity anomalies and (D) residual gravity anomalies of the final density model. (E) Modelled magnetic anomalies and (F) residual magnetic anomalies of the final magnetic susceptibility model. BB – Bjørnøya Basin, FP – Finnmark Platform, HAB – Harstad Basin, HB – Hammerfest Basin, LH – Loppa High, SB – Sørvestsnaget Basin, SH – Stappen High, SIP – Seiland Igneous Province, SR – Senja Ridge, TB – Tromsø Basin, VH – Veslemøy High.

Geological setting

Onshore rocks and offshore crystalline basement

The rocks exposed on the Norwegian mainland are described as four Caledonian nappe complexes (allochthons) overlying Precambrian autochthonous basement. The nappe complexes were described as early as 1985 by Roberts & Gee (1985). In summary, the Uppermost Allochthon is classified as an exotic terrane of Laurentian origin, the Upper Allochthon as both crust and uppermost mantle of the Iapetus Ocean with its island arcs, and the middle and lower allochthons are of pre-Caledonian and mostly of Baltican origin. The nappes are relics after the collapse of the Caledonian orogeny which formed by collision between Laurentia and Baltica in Mid Palaeozoic times (cf., Corfu et al., 2014).

Most of the mainland within the study area belongs to the Middle Allochthon and is defined as the Kalak Nappe Complex (KNC) which is bounded to the southeast by lower nappes and parautochthonous basement (B) as shown in Fig. 1 (Roberts & Gee, 1985; Corfu et al., 2014). The KNC consists mainly of Meso- to Neoproterozoic metasedimentary rocks which were metamorphosed initially during tectonic episodes at approximately 850 Ma, and from 700 to 680 Ma (Kirkland et al., 2006; Corfu et al., 2007; Gasser et al., 2015). Subsequently, the rocks of the KNC were intruded by voluminous mafic–ultramafic rocks forming the Seiland Igneous Province (SIP; see Fig. 1 for location) from 580 to 560 Ma. The emplacement of the SIP occurred in an extensional setting (Siedlecka et al., 2004; Roberts et al., 2010), after which the KNC was thrust-emplaced during the Caledonian orogeny.

In the southwestern Barents Sea, crustal models including petrology and geometry have been derived from geophysical data including onshore-offshore correlations. There is an ongoing discussion on how the Caledonian nappe boundaries continue into the offshore areas. The earliest suggestion involved a SW–NE strike of the nappe boundaries based on the trend of major sedimentary basins around and east of the Loppa High (Harland & Gayer, 1972; Gabrielsen, 1984; Doré, 1991; Gudlaugsson et al., 1998; Ritzmann & Faleide, 2007; Tsikalas et al., 2012). Interpretation of magnetic anomalies revealed a different pattern with a north-easterly strike near to the coast changing to a northerly trend east of the Loppa High (Barrère et al., 2009; Barrère et al., 2011; Gernigon & Brönner, 2012; Gernigon et al., 2014; Shulgin et al., 2020; Doré et al., 2021).

The pre-Caledonian history of the southwestern Barents Sea is less well understood. From onshore geological investigations of the Precambrian autochthonous basement it is known that the area was located at the junction of collisional regimes of differing strike directions such as the Svecofennian trend (NW–SE; Palaeoproterozoic, cf., Daly et al., 2006) and the Timanian trend (WNW–ESE; late Neoproterozoic) as found on the Varanger Peninsula (cf., Herrevold et al. 2009) and adjacent areas in NW Russia (Roberts & Siedlecka, 2002; Siedlecka et al., 2004). An offshore continuation of the roughly N–S-trending highly magnetic granitoid belt forming the Palaeoproterozoic Transscandinavian Igneous Belt (TIB) into the Loppa High area has also been suggested (Olesen et al. 2010).

Sedimentary basins

The sedimentary successions and basin development have been summarised by Smelror et al. (2009) for the entire Barents Sea. Depth maps of major sedimentary layer boundaries were presented by Klitzke et al. (2015). In the southwestern Barents Sea, the oldest documented sediments were deposited in response to rifting in Early Carboniferous to Permian times in the offshore areas of the eastern part of the study area (Gudlaugsson et al, 1998; Ritzmann & Faleide, 2007, Doré et al., 2021, Ryseth et al., 2021). This episode was followed by a westward shift of the basin development culminating in rifting in Middle Jurassic to Early Cretaceous times that generated the deep basin areas in the western part of the study area with the Tromsø Basin, Sørvestsnaget Basin and Bjørnøya Basin. Next, a further westward shift occurred and caused deposition of thick sedimentary sequences during rifting in Late Cretaceous to Paleocene times (cf., Ryseth et al., 2021). This was followed by the opening of the Norwegian–Greenland Sea in Late Paleocene to Early Eocene times (Faleide et al., 1993, 2008). The next phase of major sedimentary deposition was related to the glaciations in Pliocene–Pleistocene times. Large depositional centres developed in the westernmost part of the southwestern Barents Sea at the transition to the abyssal plain (Laberg et al., 2012, and references therein).

Phases of uplift were recognised in the sedimentary strata dated to Early Cretaceous, Late Cretaceous–Paleocene and Plio–Pleistocene times (Riis, 1986; Henriksen et al., 2011; Indrevær et al., 2016; Zieba et al., 2017 and references herein). Sedimentary erosion caused by exhumation was observed in the

eastern part of the study area and gradually decreased towards the northwest, with a transition to deposition in the areas of basin subsidence. The cumulative effect of these events was quantified by maps of net erosion and net deposition (cf., Henriksen et al., 2011).

Data, methods and workflow

Gravity anomalies are an expression of the density distribution throughout the subsurface, which is defined by the densities of the rocks and thus all their minerals and fracture/porosity fills. Magnetic anomalies express the distribution of magnetic properties in the subsurface, the origin of which is attributed to magnetic minerals. Magnetic attributes include magnetic susceptibility, which is a measure of the strength of the induced magnetisation in a rock in response to an applied magnetic field, as well as the natural remanent magnetisation (NRM). The latter is the inherent magnetization of a rock acquired at the time of its formation with possible modifications during later geological processes such as, e.g., metamorphic events. The Koenigsberger ratio is the ratio between NRM and induced magnetisation and provides an indication for the relative contribution of the NRM to the observed magnetic anomalies (cf., Dentith & Mudge, 2014).

The gravity data (Fig. 2A; Geological Survey of Norway; Olesen et al., 2010) consist of a compilation of marine free-air gravity data (sensor level at sea-level) and onshore Bouguer gravity data (correction density = 2.67 g/cm^3; sensor level at bedrock surface) with a grid cell size of 2 x 2 km. The coverage by marine gravity acquisition lines near to the shore is exceptionally sparse, and these areas were therefore filled by satellite free-air gravity data (Sandwell et al., 2014). The area enclosed by the white dotted lines in Fig. 2A marks the zone where the marine and satellite gravity data were merged. Farther offshore, the marine survey line coverage (Olesen et al., 2010) is tight but irregular, and gravity acquisition was performed at different times and with different instrumentation. This indicates a varying accuracy across the dataset. A coarse estimate of the error was derived by calculating the difference to satellite gravity anomalies (Sandwell et al., 2014). However, as satellite gravity data are of appreciably lower spatial resolution than marine gravity data, only the long-wavelength range of the calculated differences will contain information about the error. Consequently, a 3rd-order polynomial trend function was fitted to the differences highlighting the long-wavelength range. The mean value of this trend function is 3 mGal, its standard deviation is 1.3 mGal and the total span is approximately 5 mGal. This gives an indication of the magnitude of the error in the marine gravity data, which was assumed to be reasonably captured by half of the total span, i.e., an error of ± 2.5 mGal.

The aeromagnetic data (Fig. 2B) are a compilation of both vintage and more recent aeromagnetic surveys (Geological Survey of Norway (NGU): Olesen et al., 2010) with a grid cell size of 2 x 2 km and with an accuracy less than 5 nT. Sensor elevation in the offshore area is approximately 200 m above sea level and varies between 150 and 300 m above ground on land.

3D forward and inverse modelling as well as processing, filtering, profile- and map display were performed in Geosoft Oasis Montaj™ / GMSYS-3D™. The forward and inverse calculations of gravity and magnetic anomalies were performed in the wave number domain with the algorithm of Parker (1973) applying a Fast Fourier Transform (FFT; Brigham & Morrow, 1967) with an expansion factor of 100%. A further, mathematically different, modelling approach was applied using Encom ModelVision™. Here, the anomalies were precisely calculated for a model consisting of vertical slabs with square-shaped horizonal top- and bottom surfaces. This alternative approach was used to check the FFT generated inversion results of this study (without finding significant discrepancies), and to perform the model calculations as described in the sections “Uncertainty” and “Rock classification method”.

The model structure of the 3D density and magnetic model was designed to capture the characteristics of the subsurface geology, but also to be simple enough to be processed in the modelling/inversion program. The model structure is shown in Fig. 3A and represents a layer stack with layer boundaries at major contrasts in densities and/or magnetic susceptibilities. It consists of the oceanic water layer, three sedimentary units L1, L2, L3, a crustal layer (crystalline crust) and a mantle layer. The layer boundaries are defined by regular grids as sketched in Fig. 3A. The layer properties (densities or magnetic susceptibilities) can be specified as a constant value for an entire layer or as a grid with laterally varying values, where each grid cell corresponds to a vertical column extending through the entire layer. The "start model" is the earliest version of the layer stack model that is modified in the modelling/inversion process to a "final model" which reproduces the gravity and magnetic anomalies to a high degree. To get reasonable results in the inversion, the start model needs to be carefully prepared based on all available constraints.

The workflow used for the development of the petrological model of the crystalline crust is outlined in Fig. 3B and provides an overview of the rather extensive work described in detail in the following sections. The workflow consists of three major steps. The first step aimed at an isolation of the gravity contribution from the crystalline crust which then was inverted for crustal densities. For this purpose, a complete density model with oceanic water layer, sedimentary units, crustal geometry, and uppermost mantle had to be constructed. Constraints for the sedimentary units included well logs of density, compaction functions, mapped net erosion and deposition, as well as known locations of salt domes. Constraints for the crustal layer included deep seismic profiles, published depth maps of top crystalline basement and Moho, as well as density ranges for crustal rocks. Mantle densities were derived from values of analogous settings.

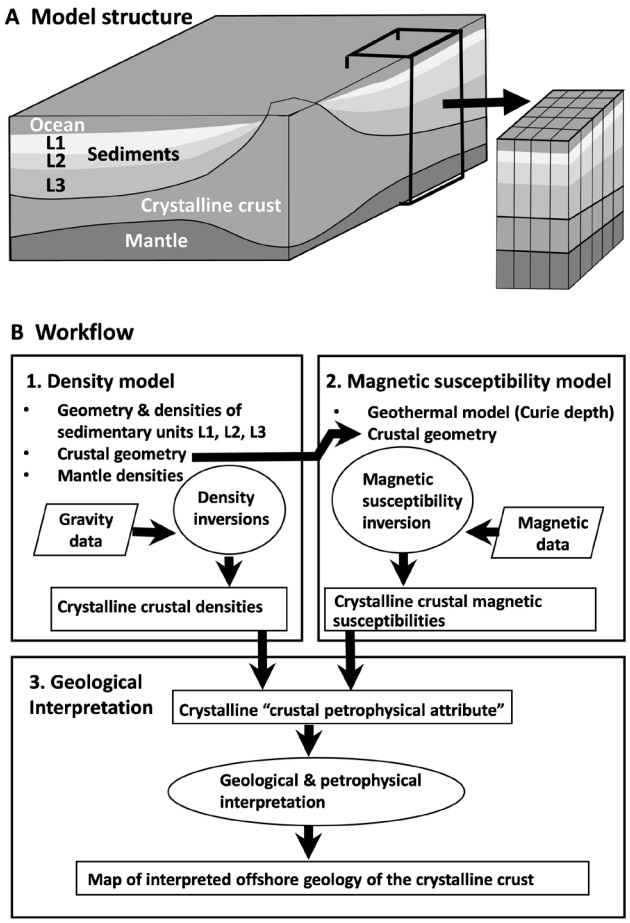

Figure 3. (A) Model structure for the gravity and magnetic field modelling and inversion. (B) Workflow for the development of the crustal petrology model.

The second step addressed the magnetic susceptibilities of the crustal layer. The magnetic anomalies were completely attributed to the crystalline crust, as both sedimentary rocks from the Norwegian Continental Shelf (Mørk et al., 2002), and pristine mantle rocks (cf., Clark, 1997) have very low magnetic susceptibilities and NRM. The magnetic layer is thus confined by the top crystalline basement derived in the first step and by an estimated depth to the Curie isotherm (see section "Crustal magnetic susceptibility model"). Magnetic inversion was performed resulting in the crustal magnetic susceptibility grid. A substantial bias on the inverted magnetic susceptibilities can be caused by NRM of sills, dykes, basalts, or crustal rocks. Such scenarios were found in the westernmost part of the study area and are addressed in chapter "Geological interpretation and discussion".

The third step aimed at the identification of the different crustal rock types. The crustal densities and magnetic susceptibilities obtained in steps 1 and 2 were interpreted using a cross-plot of published ranges of rock parameters, a modified version of the Henkel Petrophysical Plot (Henkel, 1991; Enkin et al., 2020). Furthermore, the crustal densities and magnetic susceptibilities were combined in a novel "crustal petrophysical attribute" map that allowed a preliminary classification of rock types on that map. Further constraints included published crustal seismic velocities, and published geological history and models, onshore and offshore.

Model development

Density model of sedimentary units

The uppermost layer of the density model in Fig. 3A is the oceanic water layer whose depth (Fig. 4A) is defined by the global compilation of Smith & Sandwell (1997), and whose density was set to the density of seawater with 1.03 g/cm^3 (cf., Hinze et al., 2013).

Analysis of well data showed that the densities within major sedimentary layers vary substantially across the study area (Tsikalas, 1992; Breivik et al., 1998; Ritzmann & Faleide, 2007; Barrère et al., 2009, 2011; Clark et al., 2013; Marello et al. 2013). These variations are primarily an expression of mechanical and chemical compaction that causes density to increase with depth (cf., Giles, 1997), which is further complicated by the complex geological history including uplift and erosion (see chapter "Geological setting"). Consequently, it is not possible to assign a constant density to a chronostratigraphic sedimentary layer or sequence, and a rather complex system of compaction functions would be required to correctly reflect their density-depth functions. Therefore, a different approach was chosen. For the aim of this paper a sedimentary model was needed that correctly reproduces the sedimentary gravity response, but keeps the modelling and inversion process simple. It was therefore chosen to divide the sedimentary model into three layer-shaped units named L1, L2 and L3, having either a constant density or a laterally varying density grid (Fig. 3A). The boundaries between these units do not necessarily coincide with any particular geological age or stratigraphic boundary. The stepwise change of densities with depth deviates from common sedimentary density-depth functions which increase more steadily with depth (cf., Giles, 1997) as, e.g., exponential density-depth functions (cf., Litinsky, 1989). However, this is not problematic in the interpretation of gravity data because, according to gravity theory, a function with stepwise increase of densities with depth can be transformed into a function of steadily increasing density with depth yielding the same gravity anomalies (cf., Litinsky, 1989).

Sedimentary density-depth step functions were derived from 26 density well logs (Norwegian Petroleum Directorate (NPD; factpages.npd.no, visited 11.01.2022). The units L1 and L2 were chosen to represent average densities of 2.2 g/cm^3 and 2.45 g/cm^3, respectively. The choice of these densities reflects the depth range of the wells, where a density unit with an average density of 2.45 g/cm^3 was the

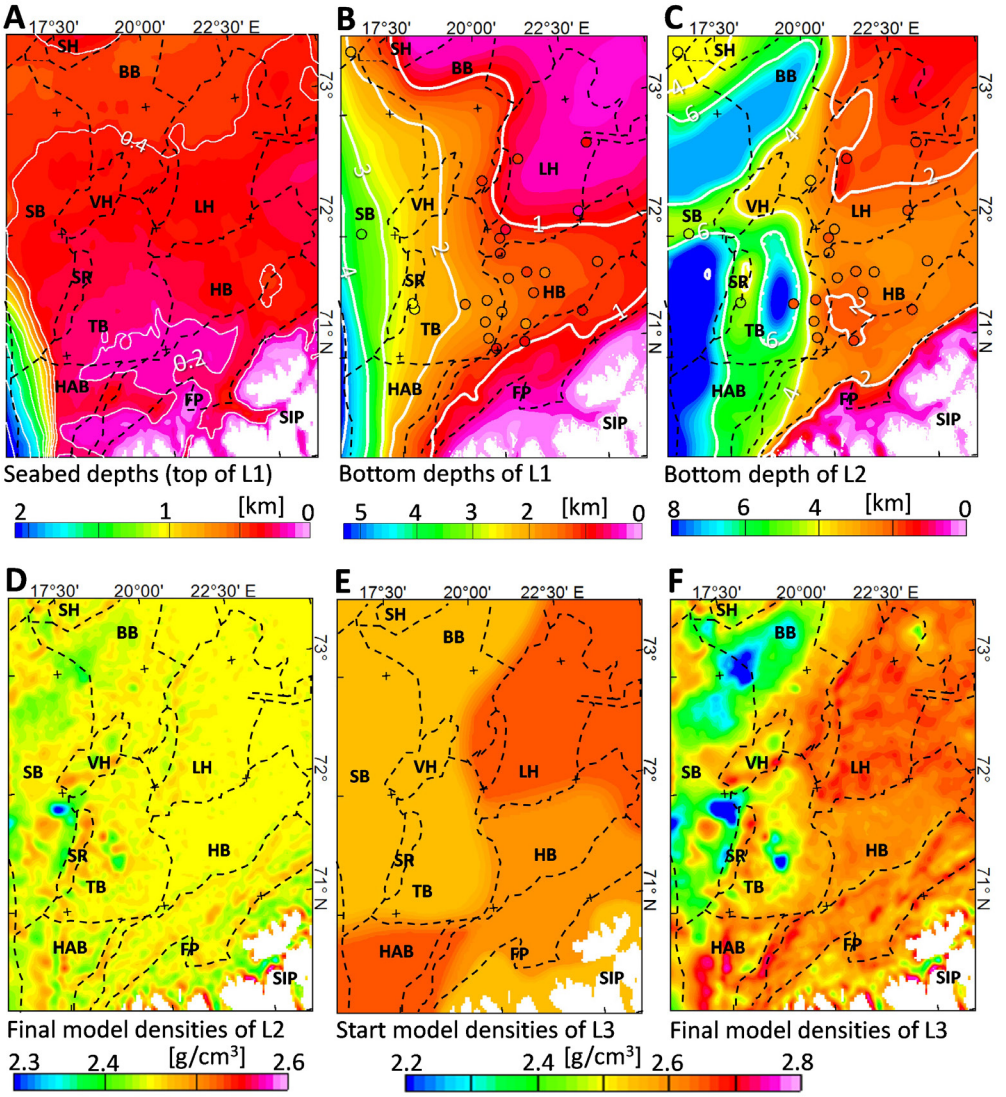

Figure 4. Sedimentary density model layers (see Table 1 for details). (A) Seabed depth (equals the top of unit L1). (B) Bottom depth of unit L1 (equals the top of unit L2) with depths derived from density well logs, shown by the coloured fill of the circles at the well locations. (C) Bottom depth of unit L2 (equals the top of unit L3) with depths derived from density well logs, shown by the coloured fill of the circles at the well locations. (D) Final model densities of unit L2. (E) Start model densities of unit L3. (F) Final model densities of unit L3. Boundaries of structural elements (black dashed, details in Fig. 1, abbreviations in Fig. 2).

deepest possible unit, that could still be reliably deduced from a larger number of wells. The estimation of the bottom depths of unit L1 and L2 was carried out as follows. The first step was to seamlessly divide the entire well density log into small depth segments in which the average density remains unchanged, ignoring the short-wavelength noise common in well data (cf., Rider, 1986). These average densities were assigned to the corresponding depth segments. In case of incomplete well logs, the lacking data were interpolated. Starting from the seabed, the density segments were joined into a larger segment required to have an average density of 2.2 g/cm^3. The base of this segment is the bottom of unit L1. Subsequently, the same procedure was applied for unit L2, but now starting at the bottom of unit L1, and aiming at an average density of 2.45 g/cm^3. The resulting bottom depths of unit L1 and L2 are shown by colour-coded circles in Fig. 4B, C, respectively. The next step was to expand the well-derived bottom depths of L1 and L2 into grids that cover the entire study area. In the western part of the study area, where the well distribution is especially scarce, additional constraints were needed to fill the gaps.

Starting with L1, support was found in the map of net erosion and net deposition (Fig. 5B; Henriksen et al., 2011; Norwegian Petroleum Directorate, 2014). Positive net erosion describes the amount of eroded and removed sediments, and where this happens, sediments from greater depth with higher compaction and consequently elevated densities will be nearer to the surface. Net deposition describes the quantity of eroded sediments that were re-deposited; these sediments will have lower compaction than at their original location and consequently lower densities (cf., Henriksen et al., 2011). The thickness of unit L1 as derived from the wells (colour-filled circles in Fig. 5A) shows a linear correlation with the value of net erosion and net deposition (Fig. 5B) as demonstrated in Fig. 5C.

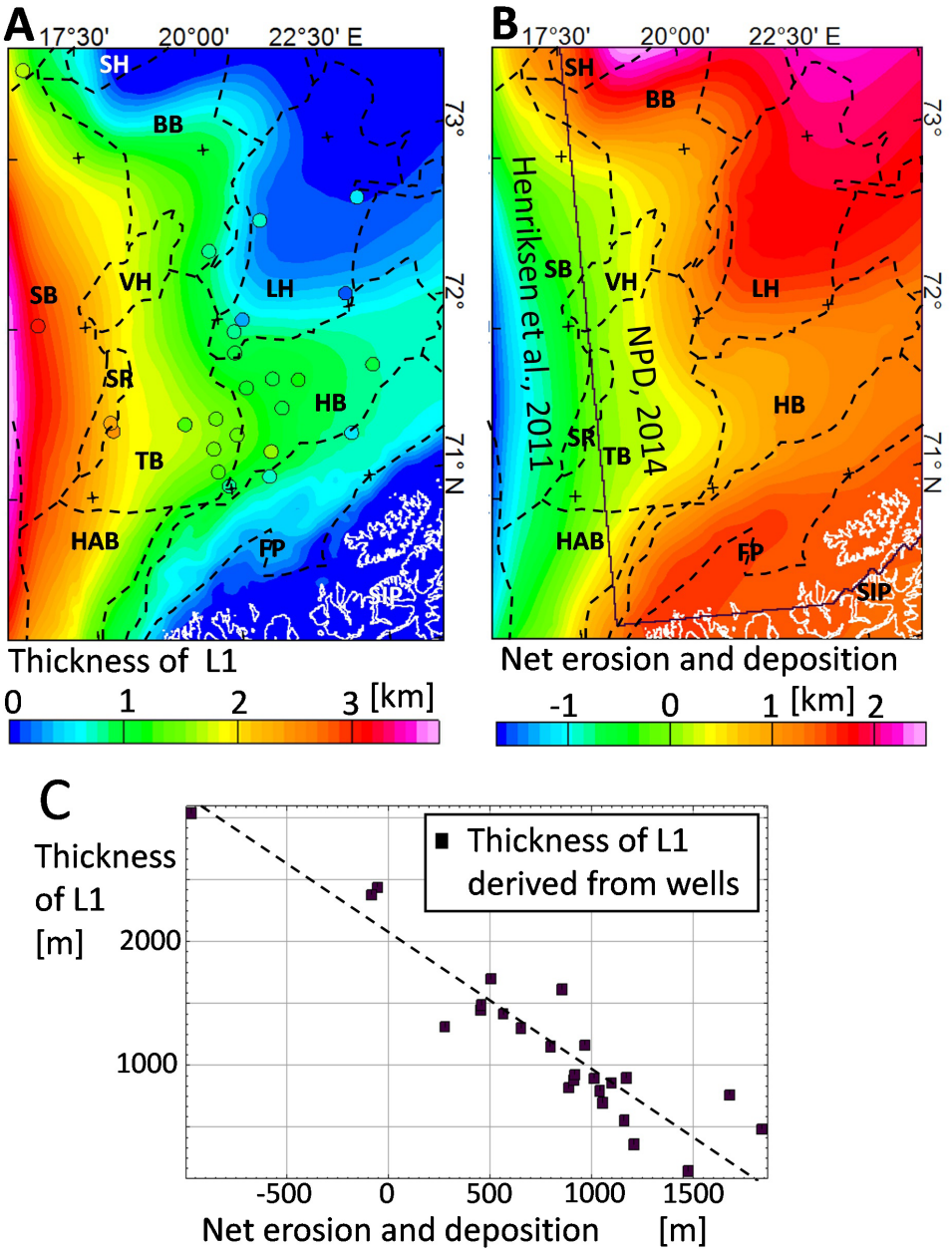

Figure 5. (A) Thickness of sedimentary unit L1 with thicknesses derived from density well logs, shown by the coloured fill of the circles at the well locations. (B) Net erosion and deposition compiled from the maps of the Norwegian Petroleum Directorate (Norwegian Petroleum Directorate, 2014) and of Henriksen et al. (2011). Boundaries of structural elements (black dashed, details in Fig. 1, abbreviations in Fig. 2). (C) Cross plot of well-derived thicknesses of unit L1 vs. net erosion and deposition with calculated linear regression line (dashed; slope = 1.0533, intercept = 2019.7 m).

The linear regression function, shown in Fig. 5C, was utilised to calculate the bottom depths of L1 outside the wells. The area that is densely covered by wells showed minor short wavelength variations which were smoothed. The well results at the Loppa High have appreciable deviations from the calculated layer thickness, possibly a result of the complex and laterally varying density structure of unevenly distributed carbonates (cf., Elvebakk et al., 2002). The thickness of unit L1 on land, where the crystalline rocks are cropping out, was set to zero and a smoothed interpolation in the near coastal area was applied. The final map of the bottom depth of L1 is shown in Fig. 4B, its thickness in Fig. 5A. Its density is constant with a value of 2.2 g/cm^3. The unit L1 was kept without changes throughout the model refinement process.

The bottom depth of L2 was derived by interpolation between the bottom depths from the wells, and in areas outside the high well coverage it was considered reasonable that it mimics the topography of the map of net erosion and deposition (Fig. 5B) in the east, and the map of the crystalline basement topography in the west (see section “Crystalline crust and mantle”). Further refinements were gained as described in the section “Model refinement of density model”. The final depth to the bottom of L2 is shown in Fig. 4C. The start model density of L2 is a constant value of 2.45 g/cm^3, that was modified as shown in section “Model refinement of density model” resulting in the final model density grid shown in Fig. 4D.

The bottom depth of unit L3 is the depth of the top crystalline basement. This sedimentary unit L3 shows a large variation in both layer thickness and in the age of the sediments (cf., Klitzke et al., 2015) which argues for the necessity of laterally varying densities. Consequently, a grid with varying densities was constructed as the start model (Fig. 4E). The lowest density (2.55 g/cm^3) was assigned to the westernmost part (Sørvestsnaget Basin, Bjørnøya Basin, Tromsø Basin), intermediate densities (2.6 g/cm^3) to the Hammerfest Basin and high densities (2.65 g/cm^3) to the Harstad Basin, Loppa High and platforms farther east. This density grid formed the start model and was adjusted as described in section “Model refinement of density model” resulting in the final model density grid of L3, shown in Fig. 4F.

The final model densities of L2 (Fig. 4D) and L3 (Fig. 4F) show several coinciding locations with low densities resembling circular and oval shapes. Such density features can be caused by gas chimneys where the sedimentary densities are lowered due to gas-filled pore space (cf., Bauer & Fichler, 2002) or by salt domes (cf., Stadtler et al., 2014). A simple test was performed to investigate whether these patterns could be related to salt. The model geometry used in this test was not intended to represent the actual geometry of potential salt domes, but merely to give an indication of the occurrence of salt and an idea of salt volume. Assuming a maximum salt scenario, all density differences between start model densities and final model densities of units L2 and L3 were solely attributed to embedded bodies with a density of 2.2 g/cm^3, which is the density of the most common salt mineral halite (cf., Dentith & Mudge, 2014). This resulted in a map of potential salt thickness (Fig. 6A). Its contour at 1800 m was superimposed on a compilation of seismically mapped salt dome boundaries (Mjelde et al., 2002; Gernigon et al., 2014; George et al., 2017) in Fig. 6B and shows a decent degree of similarity. All locations with a potential salt thickness greater than 5000 m (indicated by the yellow-red colour in Fig. 6A) coincide with locations of published salt domes. In the Sørvestsnaget Basin, similarity with sketched locations of further salt domes by Rowan & Lindsø (2017) was observed, but their sketch is extremely coarse and could not be geo-referenced. The map of potential salt thickness may therefore provide an aid to outline areas of possible occurrences of salt as well as indicate the amount of salt present. The areas enclosed by the 1800 m contour in the northern part of the Sørvestsnaget Basin and the northwestern part of the Bjørnøya Basin have not yet been reported as salt bearing. Support for the salt hypothesis was found by looking at plate reconstructions of the Norwegian–Greenland Sea. Here, the Danmarkshavn Basin off NE Greenland is a prominent salt basin (cf., Fyhn & Hopper, 2021) and in a pre-breakup reconstruction it sits en échelon with the Sørvestsnaget Basin (Lundin & Doré, 2011).

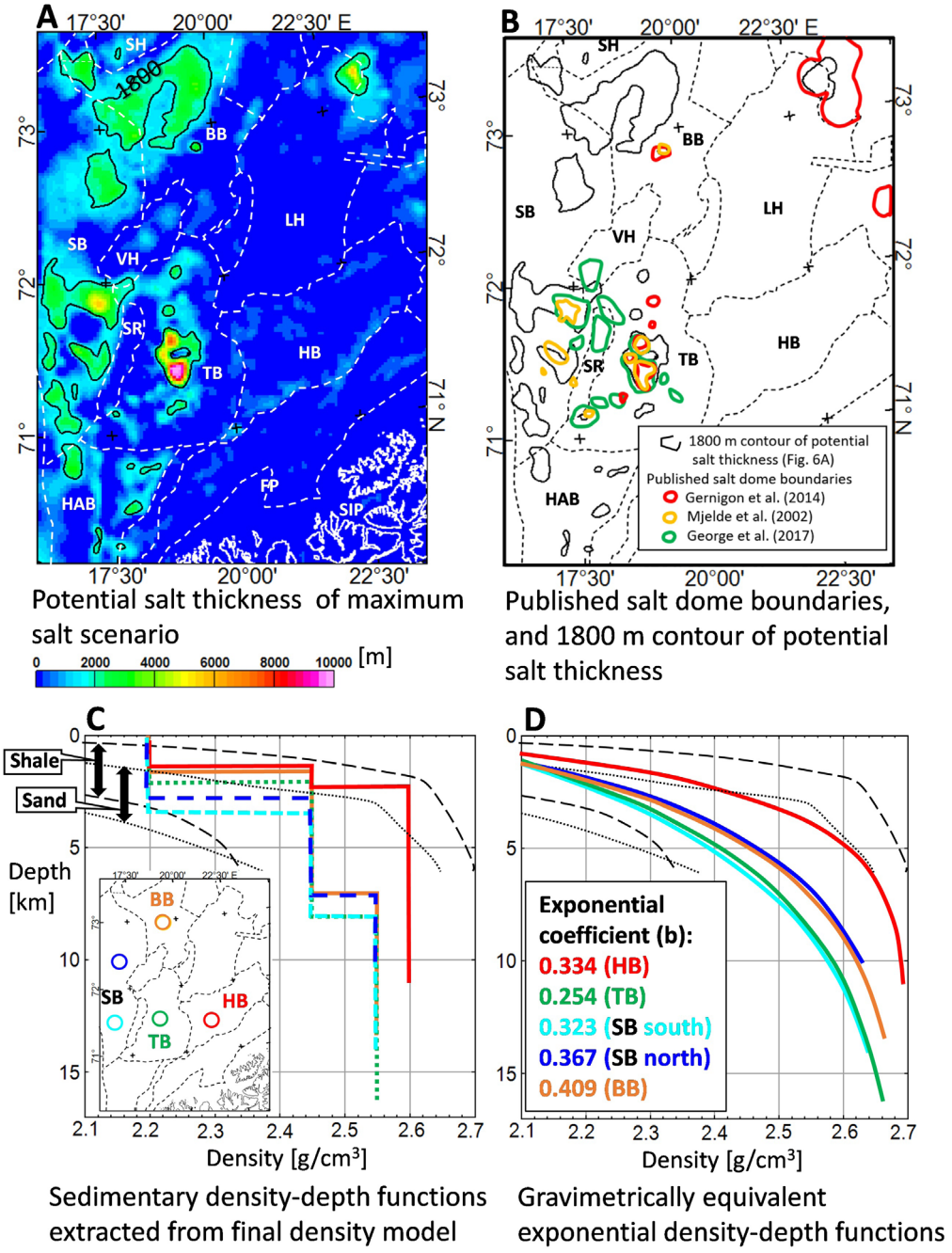

*Figure 6. (A) Potential salt thickness in a maximum salt scenario with contour line of 1800 m thickness in black, boundaries of structural elements (white dashed, details in Fig. 1, abbreviations in Fig. 2). (B) Published salt dome boundaries and 1800 m - contour line from Fig. 6A, boundaries of structural elements (black dashed, details in Fig. 1, abbreviations in Fig. 2). (C) Sedimentary density-depth step functions extracted from the final density model (Table 1) with locations in inset and (D) corresponding exponential density-depth functions, for definition of "b" see function: "Dmin + (Dmax - Dmin) * (1 - e^-b * depth); D – density". Corresponding functions in Fig. 6C and Fig. 6D have the same colour and yield the same gravity anomalies. Density ranges of global compaction curves (see text for details) are superimposed on Fig. 6C, D with black stippled lines–sandstones, black dashed lines-shales.*

Wide density depressions in the central parts of the westernmost basins (Fig. 4D, F) shown on the map of potential salt thickness between 800 and 1800 m by light blue colour in Fig. 6A, may be caused by extensive layers of salt, but alternative explanations need to be considered. A crustal origin can be excluded as shown in the section "Model refinement of density model". Lowered mantle densities beneath the Moho were suggested by Ebbing et al. (2007) but would require petrology changes or geological processes which lower the mantle densities, such as serpentinisation (cf., Escartin et al., 2001). An alternative explanation may be found in a lowered sedimentary compaction or in a change of sedimentary lithology. To test this hypothesis, sediment density-depth functions were extracted in the deep part of the westernmost basins, outside the areas enclosed by the 1800 contour of the potential salt thickness, with locations shown in inset of Fig. 6C. The resulting density-depth step functions (Fig. 6C) were converted into exponential density-depth functions applying the method of Litinsky (1989) obeying the condition that both step function and exponential function yield the same gravity anomaly. The resulting exponential functions are shown in Fig. 6D together with ranges for global observations of compaction curve ranges. The latter were obtained by conversion of porosity-depth functions (Giles, 1997) to density-depth functions with matrix densities of 2.65 g/cm^3 for sand and of 2.72 g/cm^3 for shale (Sclater & Christie, 1980). All resulting exponential functions shown in Fig. 6D fit well into the global ranges, meaning that the wide density lows can be explained by a change in sedimentary compaction or lithology and do not necessarily need salt for their explanation. A distinction between these hypotheses requires further work including seismic interpretation.

Crystalline crust and mantle

This section documents the need for revision of earlier published maps of depth to top basement (top crystalline basement) and Moho and continues with the development of revised maps that meet new constraints including seismic profiles and well data. Three published map sets with reasonable resolution within the study area were selected for evaluation and digitisation. Skilbrei (1995) compiled a top basement map from magnetic depth estimates, which was, with minor modifications, included into the map of Ebbing & Olesen (2010; Fig. 7A), who also provided a Moho depth map (Fig. 8A). Ritzmann et al. (2007) presented maps of top basement and Moho for the entire Barents Sea, derived from a regional compilation of seismic data; their data were updated and included in the more recent compilations by Klitzke et al. (2015; Figs. 7B & 8B). Barrère et al. (2011) combined industry reflection seismic data with 3D gravity and magnetic modelling which resulted in a top basement depth map (Fig. 7C) and a Moho depth map (Fig. 8C). These published top basement- and Moho depth maps capture the main structural trends associated with the basins and highs of the study area but show appreciable differences in the depth values as visible in Figs. 7 & 8.

Comparison with well data

The first step in the evaluation of the published top basement maps in Fig. 7A–C was comparison with well data (factpages.npd.no, visited 11.01.2022), some of which were recently released to the public. Five wells penetrate the basement and give a precise measure of the top basement depth; well locations are marked by white triangles in Fig. 7D. Four of these wells are located on the Loppa High and one at the boundary between the Hammerfest Basin and the Finnmark Platform. The top basement depth defined by these five wells is shallower than the depth values given in the published maps (Fig. 7A–C).

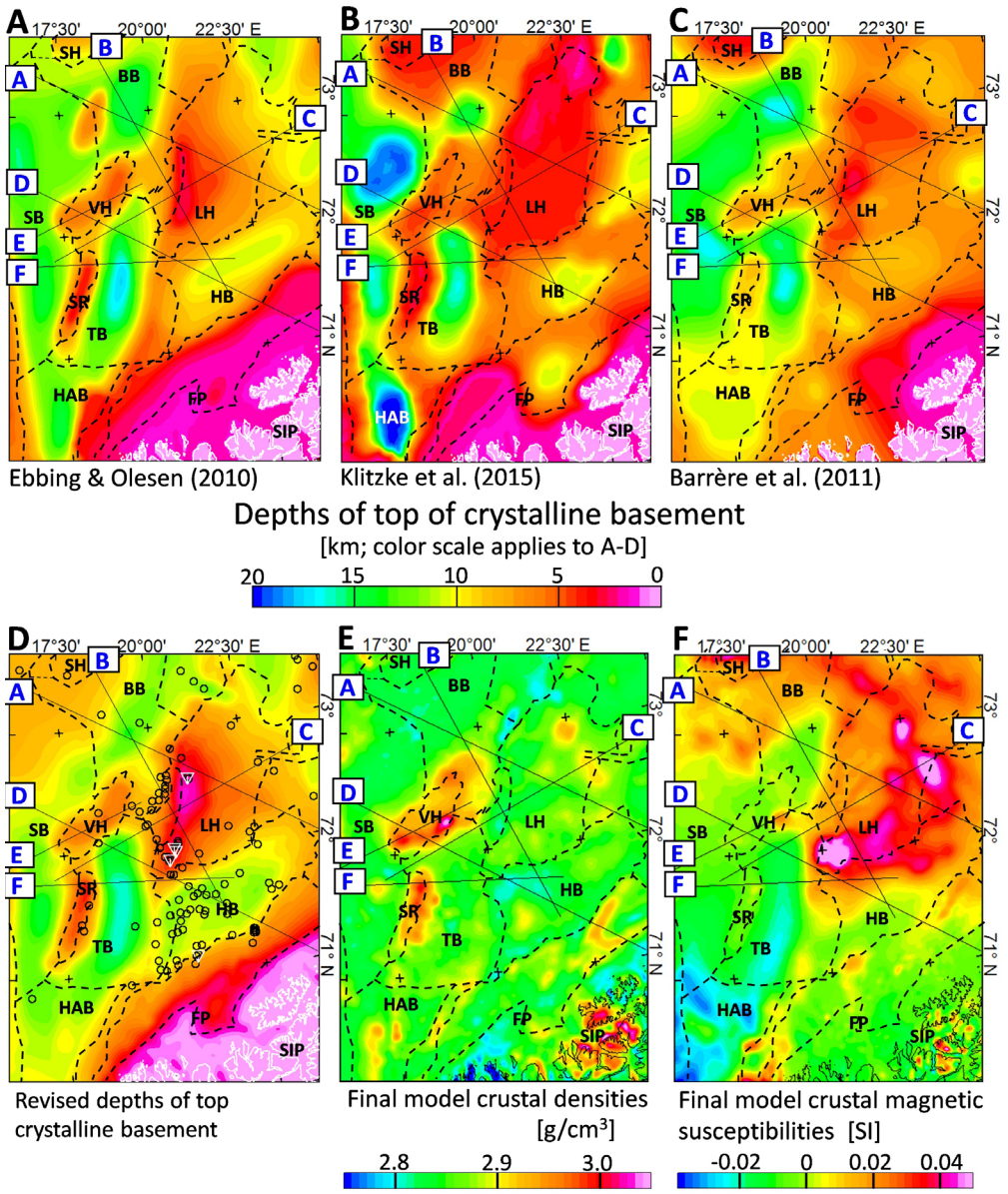

Figure 7. (A), (B) & (C) Digitised depths of the top crystalline basement from publications. (D) Revised map of depth of the top crystalline basement with locations of wells (factpages.npd.no, visited 11.01.2022), penetrating the crystalline basement (white triangles), and other wells with termination depth in the sediments (black circles). (E) Final model grid of (crystalline) crustal densities. (F) Final model grid of (crystalline) crustal magnetic susceptibilities. Boundaries of structural elements (black dashed, details in Fig. 1, abbreviations in Fig. 2), seismic profiles (black lines, details in Fig. 1).

All other wells drilled in the study area, marked by a black circle in Fig. 7D, terminate within the sediments and give an upper limit for the shallowest possible depth of the top basement. The well results were incorporated into the revised map of top basement depths (Fig. 7D). It was noted, that the well termination depths are shallower than all top basement depth values of Ebbing & Olesen (2010) and of Barrère et al. (2011), whereas the top basement depth values of Klitzke et al. (2015) are shallower than the well termination depth at well 7117/9-2 (71°22'51.05''N, 17°56'5.76''E) by approximately 2000 m and at well 7121/1-1R (71°56'25.74''N, 21°4'36.52''E) by approximately 1000 m.

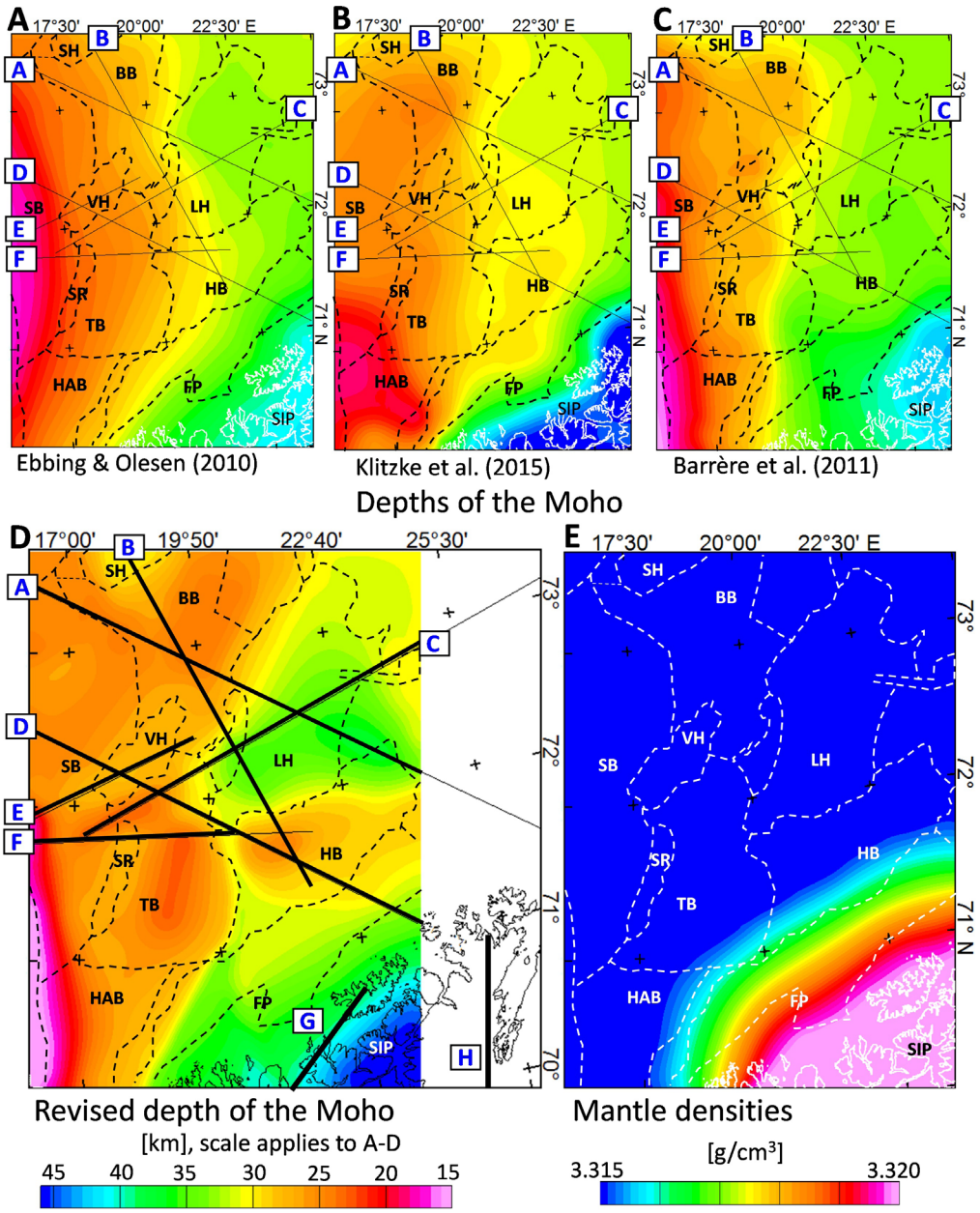

Figure 8. (A), (B) & (C) Digitised depths of the Moho from publications. (D) Revised map of the depth of the Moho. Boundaries of structural elements (black dashed, details in Fig. 1, abbreviations in Fig. 2), seismic profiles (A–F, black lines, details in Fig. 1) and refraction seismic profiles on/near land by Chroston et al. (1976; profile G) and the FENNOLORA profile (Lund, 1987; Guggisberg et al., 1991; profile H). (E) Final model densities of the mantle, boundaries of structural elements (white dashed, details in Fig. 1, abbreviations in Fig. 2).

Comparison with deep seismic profiles

The next step was the comparison of the published top basement depth maps with six seismic profiles shown in Figs. 9 & 10: (A) deep seismic reflection profile Petrobar7 (Clark et al., 2013), (B) deep seismic reflection profile NBR07-232948 (Gernigon et al., 2014), (C) Ocean Bottom Seismometer (OBS) profile 1 (Aarseth, 2018), (D) line drawing of deep seismic reflection profile IKU-C (Ritzmann & Faleide, 2007), (E) Ocean Bottom Seismometer profile OBS-A (Mjelde et al., 2002), (F) seismic reflection profile composite WBS-4/7142 (Breivik et al., 1999) with revised interpretation of Faleide et al. (2008). The crustal layer geometry from the seismic profiles is compared in Fig. 9 with the top basement and Moho depths

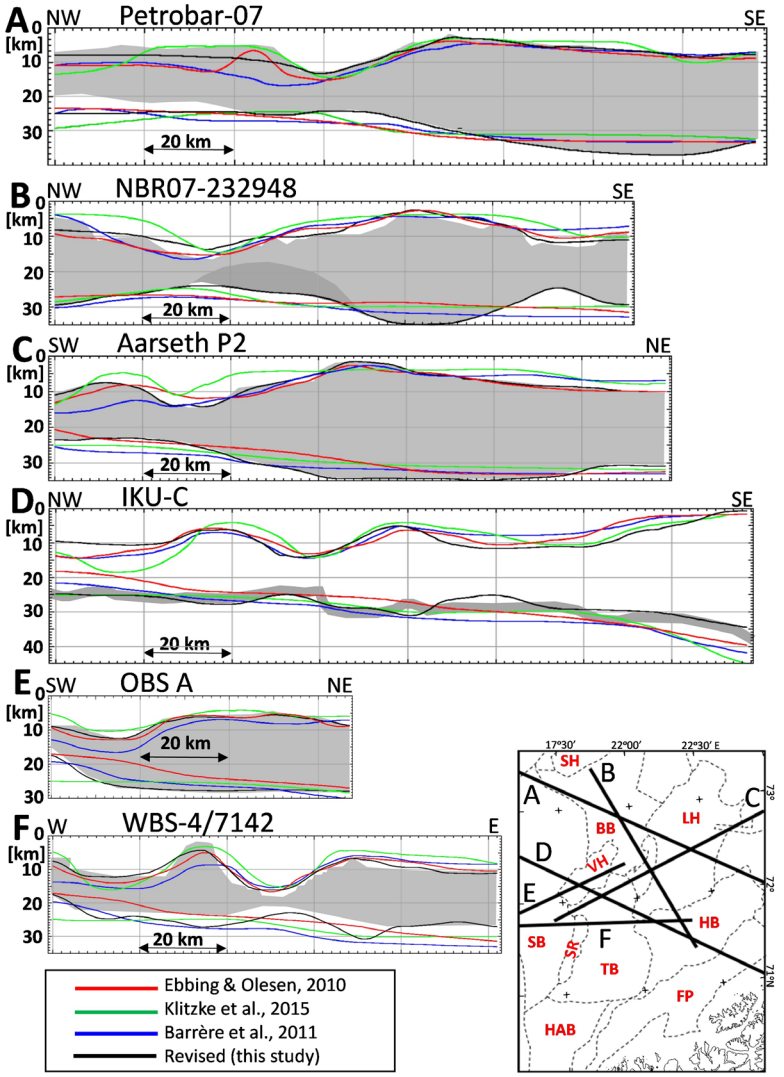

Figure 9. Comparison of published and revised top crystalline basement and Moho depths extracted along the seismic profiles, grey area is the crustal layer as defined by the seismic profiles. Profile D (IKU-C) lacked a top crystalline basement interpretation in Ritzmann and Faleide (2007). Inset with location of seismic profiles (black lines, details in Fig. 1), boundaries of structural elements (black dashed, details in Fig. 1, abbreviations in Fig. 2).

that were extracted from the published maps (Figs. 7 & 8). The deviations seen for the top basement are in the range of a few kilometres in the eastern part of the study area and reach up to 10 km in the Sørvestsnaget Basin. However, deviations are not unexpected as the publication dates of OBS Line 1 (profile C) and NBR07-232948 (profile B) postdate the publication of the evaluated top basement maps. Profile D (IKU-C) had no top basement interpretation given in Ritzmann & Faleide (2007).

It was further investigated whether the top basement and Moho depths of the seismic profiles coincide at the cross points. For this purpose, white circles were added to the profiles at the corresponding locations in Fig. 10 and only minor mismatches were found.

The top basement depths of Ebbing & Olesen (2010; red line in Fig. 9) show the smallest mismatch to the seismically mapped top basement reflectors and were therefore used as the start model for the development of a new revised top basement map. This map was adjusted to meet the top basement depth values from wells and seismic profiles. Adjustments cannot just be applied to an isolated point or to a line but need to be continued into the map plane. Such continuations were performed in alignment with the trends of the gravity anomalies, e.g., sudden changes were not applied without an indication for a sudden change in the gravity anomaly maps.

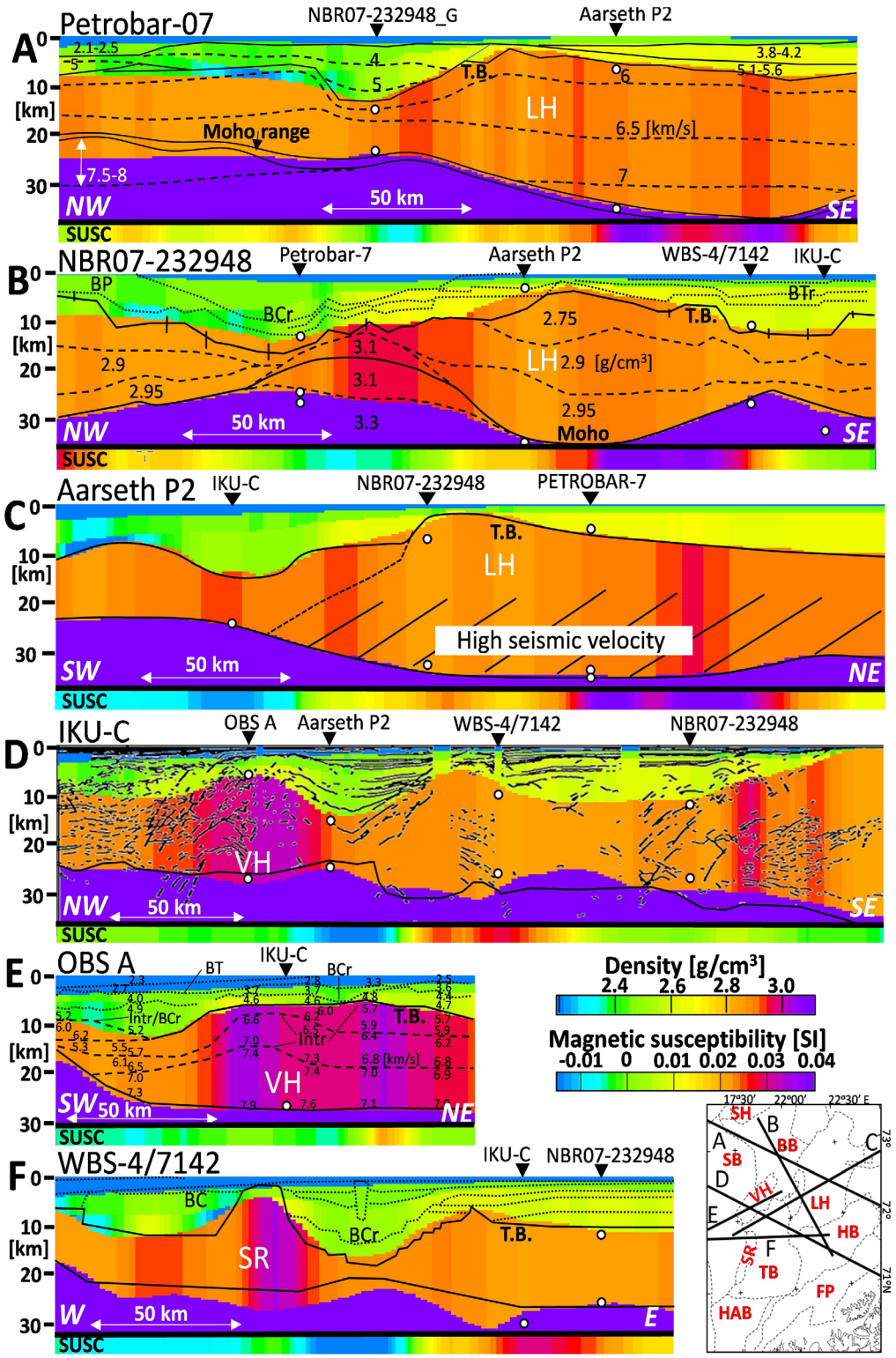

Figure 10. Sedimentary and crustal densities superimposed on the seismic profiles as extracted from the final density model (Table 1). Crustal magnetic susceptibilities (SUSC) are shown on the bar below the profiles as extracted from the final model of the crustal magnetic susceptibilities (Fig. 7F). (A) Petrobar-07 (Clark et al., 2013), black numbers–seismic velocities [km/s]. (B) NBR07-232948 (Gernigon et al., 2014), vertical black lines on the T.B. (top crystalline basement) reflector mark uncertainties, black numbers–densities [g/cm³]. (C) OBS Line 1 (Aarseth, 2018). (D) IKU-C (Ritzmann & Faleide, 2007), black lines–line drawings. (E) OBS A (Mjelde et al., 2002), black numbers–seismic velocities [km/s]. (F) WBS-4/7142 (Breivik et al., 1999; Faleide et al., 2008). BT – Base Tertiary, BC – Base Cenozoic, BCr – Base Cretaceous, BTr – Base Trias, BP – Base Permian, T.B. –top crystalline basement, Intr-Magmatic intrusions. At cross points between the seismic profiles, white circles mark the top crystalline basement and Moho depths of the crossing profile. Inset with seismic profiles (black lines, details in Fig. 1), boundaries of structural elements (black dashed, details in Fig. 1, abbreviations in Fig. 2).

A smooth interpolation was applied between the coastline which terminates the exposed top basement on land and top basement depth in the Hammerfest Basin. In areas far away from the seismic profiles, the top basement map of Ebbing & Olesen (2010) was kept unchanged. Further refinements were gained as described in the section "Model refinement of density model". The revised depth map of the top basement is shown in Fig. 7D.

The Moho depths were extracted from the published maps (Fig. 8A–C) along the seismic profiles and agree in the main trends with deepening of the Moho towards the east but show otherwise appreciable differences of up to 10 km as seen in Fig. 9. Furthermore, the Moho topography is generally smoother than on the seismic sections. Therefore, a new Moho depth map was constructed constrained by the seismic Moho reflectors from the seismic profiles. Additional constraints were found in the Moho depths from refraction seismic profiles across the Seiland Igneous Province (profile G, Fig. 8D; Chroston et al., 1976), with depths varying from 45 to 38 km from southwest to northeast, and finally, by the FENNOLORA refraction seismic profile (profile H, Fig. 8D; Lund, 1987; Guggisberg et al., 1991) which indicated a constant Moho depth of approximately 45 km; see Fig. 8D for profile locations. The Moho depth at the COB on profile E and profile F is almost coincident and the mean of these Moho depths was applied along the COB within the study area. The areas of the Moho depths unconstrained by seismic profiles were interpolated following the published Moho maps (Fig. 8A–C) with a smooth transition from the constrained into the unconstrained areas. Further refinements were gained as described in the section "Model refinement of density model". The revised depth map of the Moho is shown in Fig. 8D.

Mantle densities

The mantle layer is the deepest layer of the model and its top is confined by the Moho (Fig. 3A). The depth to the bottom of the density model and the mantle densities were chosen according to interpretations of geologically analogous settings providing that their mantle densities were calculated by the methodology of Afonso et al. (2008) which combines petrology, metamorphic processes, and geophysical inversion. The bottom of the model was set to a depth of 100 km, which corresponds to the model of the Namibian volcanic margin (Fernàndez et al., 2010). The mantle densities (Fig. 8E) were set to 3.315 g/cm^3 in the offshore areas, a value consistent with both the average densities of the Namibian volcanic margin (Fernàndez et al., 2010) and those of the continental shelf and adjacent mainland of southern Norway (Gradmann et al., 2013). Earlier studies used similar mantle densities for the southwestern Barents Sea (Barrère et al., 2011; Clark et al., 2013). Archaean crust is encountered in the southeastern part of the study area (cf., Artemieva et al., 2006), where the value of 3.320 g/cm^3 consistent with the values of the Namibian Archaean mantle (Fernàndez et al., 2010) was applied. A smooth transition was applied between the areas of different densities.

Model refinement of density model

The work described in the previous sections provided the necessary information to compile the "start model", which is the complete layer stack model (Fig. 3A) with its layers and densities listed in Table 1. The next step was to refine this model utilising 3D inversion of the gravity anomalies with the goal of creating the "final model" that would consist of geologically meaningful densities and geometries and fit the observed gravity anomalies (Fig. 2A). Minor adjustments were applied to the depth of bottom of layer L2, top crystalline basement and Moho. The further refinement focused on the density grids of the crystalline crust and sedimentary units L2 and L3 in an iterative workflow. The workflow started with an inversion for the crustal density grid meaning, that changes to the start model were only allowed by changes in the crustal density grid. The inversion of the start model resulted in reasonable crustal

Table 1. Layer stack model prior (start model) and after the gravity / magnetic inversions (final model).

Model layers	Top of layer	Bottom of layer	Densities [g/cm³]	Magnetic susceptibilities [SI]
Oceanic layer	Sea level	Seabed (Fig. 4A)	1.03	0
Sedimentary unit L1	Seabed (Fig. 4A)	Bottom of L1 (Fig. 4B)	2.2	0
Sedimentary unit L2	Top of L2 (Fig. 4B)	Bottom of L2 (Fig. 4C)	Start model: 2.45 Final model: 2.285–2.595 (grid, Fig. 4D)	0
Sedimentary unit L3	Top of L3 (Fig. 4C)	Top basement (Fig. 7D)	Start model: 2.55–2.65 (grid, Fig. 4E) Final model: 2.2–2.775 (grid, Fig. 4F)	0
Crystalline crustal layer	Top basement (Fig. 7D)	Moho (Fig. 8D)	Start model: 2.75 Final model: 2.75–3.1 (grid, Fig. 7E)	Start model: 0 Final model: -0.03–0.06 (grid, Fig. 7F)
Mantle layer	Moho (Fig. 8D)	100 km	2.315–3.32 (grid, Fig. 8E)	0

densities, apart from too low values in the deep basin areas of the Bjørnøya Basin and the Sørvestsnaget Basin. It was therefore necessary to take a closer look at crustal densities with respect to the applied model structure (Fig. 3A). Common crustal densities fall in the range between 2.65 g/cm³ and 3.4 g/cm³ (cf., Hinze et al., 2013), but this range is narrower for Caledonian and Precambrian rock averages in onshore northern Norway (2.725 to 2.9 g/cm³; Olesen et al., 2010) which are assumed to continue into the offshore areas. Nevertheless, high densities of up to 3.4 g/cm³ were found in the Seiland Igneous Province (Pastore et al., 2016).

In the applied model structure, each grid cell of the crustal density grid represents the cumulative expression of varying densities from top (crystalline) basement to Moho in a single density value (Fig. 3A). This density value is representative of the true rock density only in the case of a homogeneous crust. However, crustal densities are generally expected to increase with depth due to increasing pressure and metamorphic degree (cf., Herzberg et al., 1983). In the problematic area of the Bjørnøya Basin and Sørvestsnaget Basin, the increase in crustal seismic velocities in profile A (Fig. 10A; Clark et al., 2013) indicates an increase in crustal densities according to the well-established relationship between seismic velocities and densities (cf., Dentith & Mudge, 2014). The geometry of this area with wide regions of near-horizontal layering can be treated as a 1D model, and consequently, the crustal grid density will represent the arithmetic average of the true crustal densities from top basement to Moho. In a simple crustal scenario consisting of an upper crustal layer with a density of 2.725 g/cm³ (lower limit in the compilation of Olesen et al., 2010) and a lower crustal layer with a density of 2.9 g/cm³ (cf., Herzberg et al., 1983), and both crustal layers having the same thickness, an arithmetic mean of the densities was calculated to be 2.8125 g/cm³. A corresponding crustal scenario is encountered in the Bjørnøya Basin as seen on profile A (Fig. 10A). However, as it cannot be ruled out that the upper crust has even greater thicknesses locally, the lower limit of geologically reasonable crustal grid densities was set to 2.8 g/cm³.

The model refinement started therefore with the correction of all crustal densities that were lower than 2.8 g/cm^3 to a value of 2.8 g/cm^3. A recalculation of the gravity anomaly of this updated model resulted in a negative gravity mismatch indicating a mass deficit in either mantle or sediments. It was found that a mass deficit in the sediments is a probable scenario, as it can be explained by a combination of lowered sedimentary compaction combined with the presence of salt as shown in the section "Density model of sedimentary units".

Consequently, the model refinement allowed modifications of the start model densities of sedimentary units L2 (2.45 g/cm^3) and L3 (Fig. 5E) except for the areas constrained by well data. The lowermost acceptable sedimentary density was set to the density of the salt mineral halite (2.2 g/cm^3). In the first iteration, the gravity mismatch was attributed to L3. The inversion for the sedimentary grid densities locally yielded values that were less than 2.2 g/cm^3. The latter were corrected to 2.2 g/cm^3. A new gravity forward calculation resulted in a minor mass deficit, which was attributed to L2. Further inversion for the grid densities of L2 yielded values that were all higher than 2.2 g/cm^3. The order of inversions for the layer densities of L2 and L3 could be reversed, meaning that at the most the mass deficit (salt) would have been placed in L2 instead of L3. A distinction between these scenarios cannot be performed by the gravity method due to its inherent ambiguity (cf., Dentith & Mudge, 2014).

The layers of the final layer stack density model (Fig. 3A) are listed in Table 1. Fig. 10 shows the final sedimentary and crustal densities extracted along the seismic profiles. The calculated gravity anomalies of this model are shown in Fig. 2C and the difference between modelled and observed anomalies (residuals) in Fig. 2D. The calculated anomalies show a high degree of similarity to the observed data. The uncertainty of the crustal grid density model is discussed in section "Uncertainty".

Crustal magnetic susceptibility model

The magnetic anomalies were attributed to the crustal layer between top (crystalline) basement and ultimately the depth of the Curie temperature (T_c). At T_c depths, the rocks radically change their magnetic behaviour and can be treated as non-magnetic (cf., Hinze et al., 2013). The T_c varies for different magnetic minerals, but here we focus on magnetite with an average T_c of 580°C. Magnetite, with its high abundance in common crustal rocks and its high magnetic susceptibility, is a dominant contributor to many of the magnetic anomalies of crustal rocks (cf., Grant, 1985). Oceanic mafic and ultramafic rocks, by global measurements, have T_c values between 500° and 600°C (Zhao et al., 2006). It was therefore assumed reasonable to apply a T_c range between 500° and 600°C for the study area. If the T_c depth is deeper than the Moho, the Moho will commonly be the lower boundary of the magnetic crust as pristine mantle rocks have very low magnetic susceptibilities and NRM (cf., Clark, 1997).

It was investigated whether the T_c depth range of 500°–600° C overlaps with crustal depths. Breivik et al. (1999) applied 2D finite-element temperature modelling, but without crustal radiogenic heat production, along profile F. According to their model, the T_c depth range would correspond to 47–55 km in the east, and to 28–35 km in the west. This is clearly below the Moho (Fig. 10F). A more recent thermal model including radiogenic heat production by Brönner et al. (2010) along profile B resulted in a T_c depth range of 21–29 km below the Bjørnøya Basin and of 27–34 km below the Loppa High. This model agrees on a large scale with the superregional low-resolution thermal model of Klitzke et al. (2016). All these thermal models indicate that the 600° C isotherm is clearly below the Moho within the entire study area, whereas the 500° C isotherm may cut into the deepest parts of the crust. In the lack of a more precise T_c isotherm, the Moho was used as the lowermost boundary of magnetic rocks in this study.

The crustal layer between top crystalline basement depth and Moho depth (Figs. 7D & 8D) was inverted for the magnetic susceptibilities required to reproduce the aeromagnetic data (Fig. 2B). The inversion resulted in the final crustal magnetic susceptibility grid shown in Fig. 7F. The calculated magnetic anomalies of this model are shown in Fig. 2E together with the difference between observed and calculated magnetic anomalies (residuals) in Fig. 2F. The calculated anomalies show a high degree of similarity to the observed aeromagnetic data which is reflected by small residuals. The NRM of the crustal rocks is not captured in this approach and may – where prominent – bias the calculated crustal magnetic susceptibilities. This problem was addressed in the chapter "Geological interpretation and discussion".

Uncertainty

The error in the final crustal densities and magnetic susceptibilities is a consequence of (1) the error in the gravity and magnetic data, (2) the quality of the inversion, and (3) the uncertainty in the depth of the top crystalline basement and the Moho. The corresponding errors in crustal density and magnetic susceptibility values were calculated by model variations using 3D forward modelling. More information about the sources of the errors is given as follows, and the resulting errors are listed in Table 2.

Table 2. Error sources and error estimation of crustal densities and magnetic susceptibilities.

Origin of error	Error	Modelled error of crustal density [g/cm^3]	Modelled error of crustal magnetic susceptibility [SI]
(1) Error due to acquisition and processing	Gravity: ± 2.5 mGal Magnetic: ± 5 nT	± 0.01	± 0.001
(2) Difference between inverted and observed anomalies (Residuals)	Gravity residual: Mean value: 0.006 mGal Standard deviation: 1.6 mGal Magnetic residual: Mean value: 0.8 nT Standard deviation: 23 nT	± 0.0065	± 0.0046
(3) Error in depths to top crystalline basement and Moho	±10 % Scenario: Top basement depth / Moho depth: A: 2 km / 30 km B: 10 km / 20 km	 ± 0.0005 ± 0.0175	 ± 0.00035 ± 0.001
Sum of errors (1)+(2)+(3)	Scenario: Top basement depth / Moho depth: A: 2 km / 30 km B: 10 km / 20 km	 ± 0.017 ± 0.034	 ± 0.00595 ± 0.0066

(1) Errors caused by acquisition and processing are described in the section “Data, methods, and workflow”.

(2) The quality of the inversion is expressed by the mean value and standard deviation of the residual anomalies, defined as the difference between the modelled and the observed anomalies (Fig. 2D, F). The mean values are small compared to the standard deviations, so the error was derived from the standard deviations.

(3) It was assumed that the uncertainty in the depths of the top basement and the Moho is reasonably captured with an uncertainty of ± 10%. This uncertainty leads to errors in the crustal density and magnetic susceptibility values. This error, which is the difference between the crustal parameters before and after modifying the depths of the top basement and Moho, was calculated using 3D forward modelling. Two scenarios were examined, reflecting completely different settings: Scenario A (e.g., Loppa High) with a top basement depth of 2 km (uncertainty ± 0.2 km), and a Moho depth of 30 km (uncertainty ± 3 km); and Scenario B (e.g., westernmost basins of the study area) with a top basement depth of 10 km (uncertainty ± 1 km) and a Moho depth of 20 km (uncertainty ± 2 km). The largest error in the crustal densities and magnetic susceptibilities resulted from scenario B.

Rock classification method

The resulting crustal density and magnetic susceptibility grids (Fig. 7E, F) provided the input to the rock classification which was based on comparison with density and magnetic susceptibility ranges of common crustal rocks. These ranges were plotted into a cross plot (Fig. 11A), where density ranges refer to Hinze et al. (2013) and magnetic susceptibility ranges to Clark (1997). This style of diagram shows similarities with the Henkel Petrophysical Plot (Henkel, 1991; Enkin et al., 2020), but more rock types were included here. Furthermore, the cross plot was coloured by a grid with 20 different colours, where each colour represents a combination of certain density and magnetic susceptibility ranges. The colour setting was chosen to highlight areas of different crustal petrology and limited to the values observed in the crustal density and magnetic susceptibility grids. This cross plot will be referred to as the "modified Henkel Petrophysical Plot" (mHPP).

In the next step, a novel “crustal petrophysical attribute” map was created combining the crustal density and magnetic susceptibility grids (Fig. 7E, F) into a single map with a two-dimensional colour scale, having densities and magnetic susceptibilities on its axes. Its colour scale is defined by the colour setting of the mHPP. The resulting map is shown in Fig. 12C. The colour cells were assigned identification numbers. Note that the classes of the lowermost magnetic susceptibilities (lowest row in colour scale) have no lower limit and may thus include negative values. Negative susceptibilities may indicate a bias by remanent magnetisation, which is discussed in the section "Western Bjørnøya Basin, Sørvestsnaget Basin, Harstad Basin, and Western Tromsø Basin".

The crustal petrophysical attribute map (Fig. 12C) provided the basis for the further interpretation together with the crustal density and magnetic susceptibility grids which were displayed with a specific colour scale (Rainbow, Geosoft Oasis Montaj™; Fig. 12A, B) chosen to enhance characteristic patterns.

Further considerations are required before using this new system to identify rock types. Since each individual grid point value in the crustal density and magnetic susceptibility grids represents the entire crystalline crust, this grid point value can only be directly interpreted for rock types in the case of homogeneous crust. In the case of a 1D scenario, which means a setting without lateral changes, and with vertical density variation, the crustal grid parameters represent the arithmetic

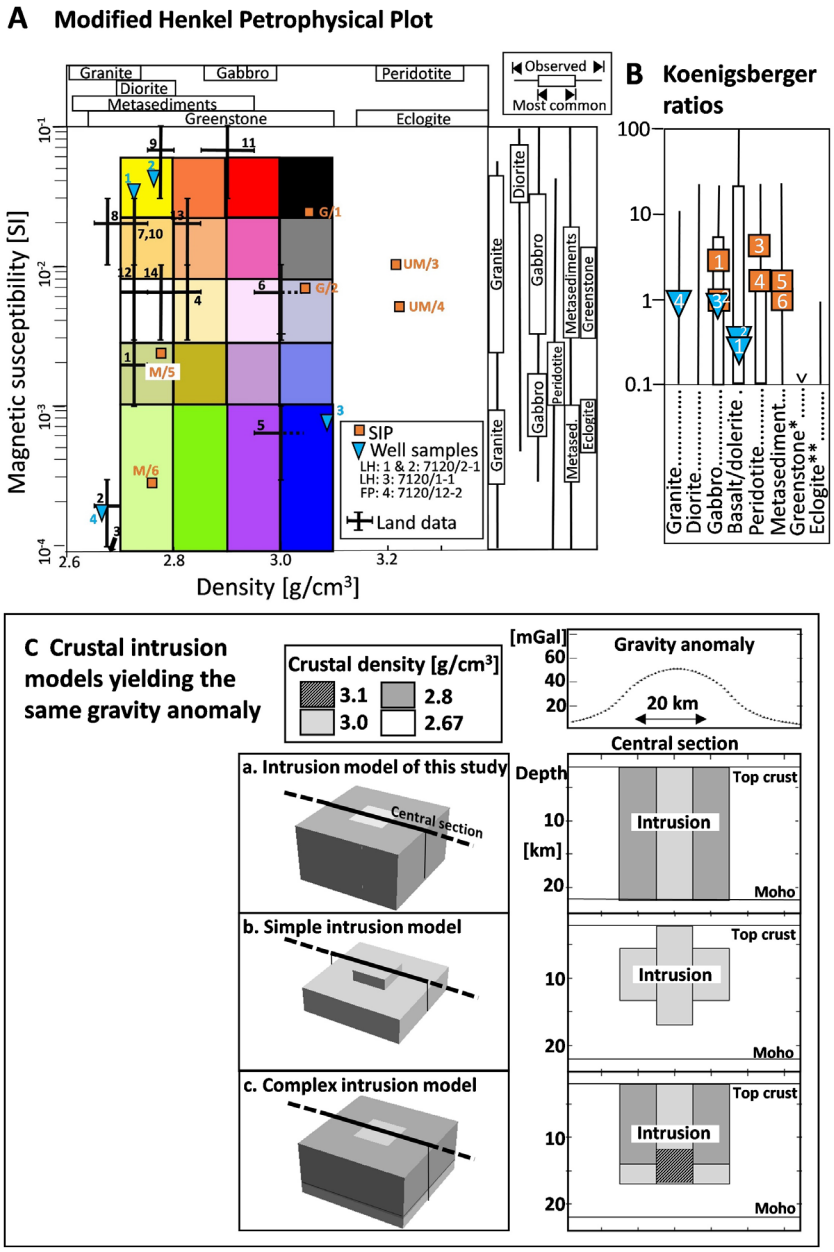

Figure 11. (A) Modified Henkel Petrophysical Plot (mHPP) with ranges of rock densities (Hinze et al., 2013) and magnetic susceptibilities (Henkel, 1991; Enkin et al., 2020; Clark, 1997; Olesen et al., 2010), rocks of the adjacent mainland (location by numbers in Fig. 13C; Table 3), crustal well cores (location by red and blue triangles in Fig. 13A; Table 3), and average values from the SIP–Seiland Igneous Province (Pastore et al., 2018; Table 3). (B) Koenigsberger ratios (Clark, 1997) with additional values from northern Scandinavia marked by "" (Olesen et al., 2010) and by "**" (Henkel, 1991). (C) Different (crystalline) crustal density models which yield the same gravity anomaly (calculated at mean sea level).*

average of the true crustal parameters. More complex settings need a more differentiated approach. The geometry of the distribution of the density and magnetic susceptibilities can be classified according to potential field theory by the structural index (N). The inverse of the structural index reflects the rate of decrease in the amplitude of the gravity or magnetic field response with increasing depth of the source (cf., Dentith & Mudge, 2014). Scenarios with circular and near-circular patterns (3D scenarios), often found for crustal intrusions, can be described by a structural index of N = 2 for gravity and N = 3 for magnetic interpretation. Consequently, the effects of the deeper crustal rocks are attenuated, and the crustal grid values gained by the inversion will predominantly represent the crustal rocks' values near to the surface. Fig. 11C takes a closer look at simple 3D scenarios with intrusions applicable for this study. Model [a] represents the intrusion by a laterally varying density with the maximum in the

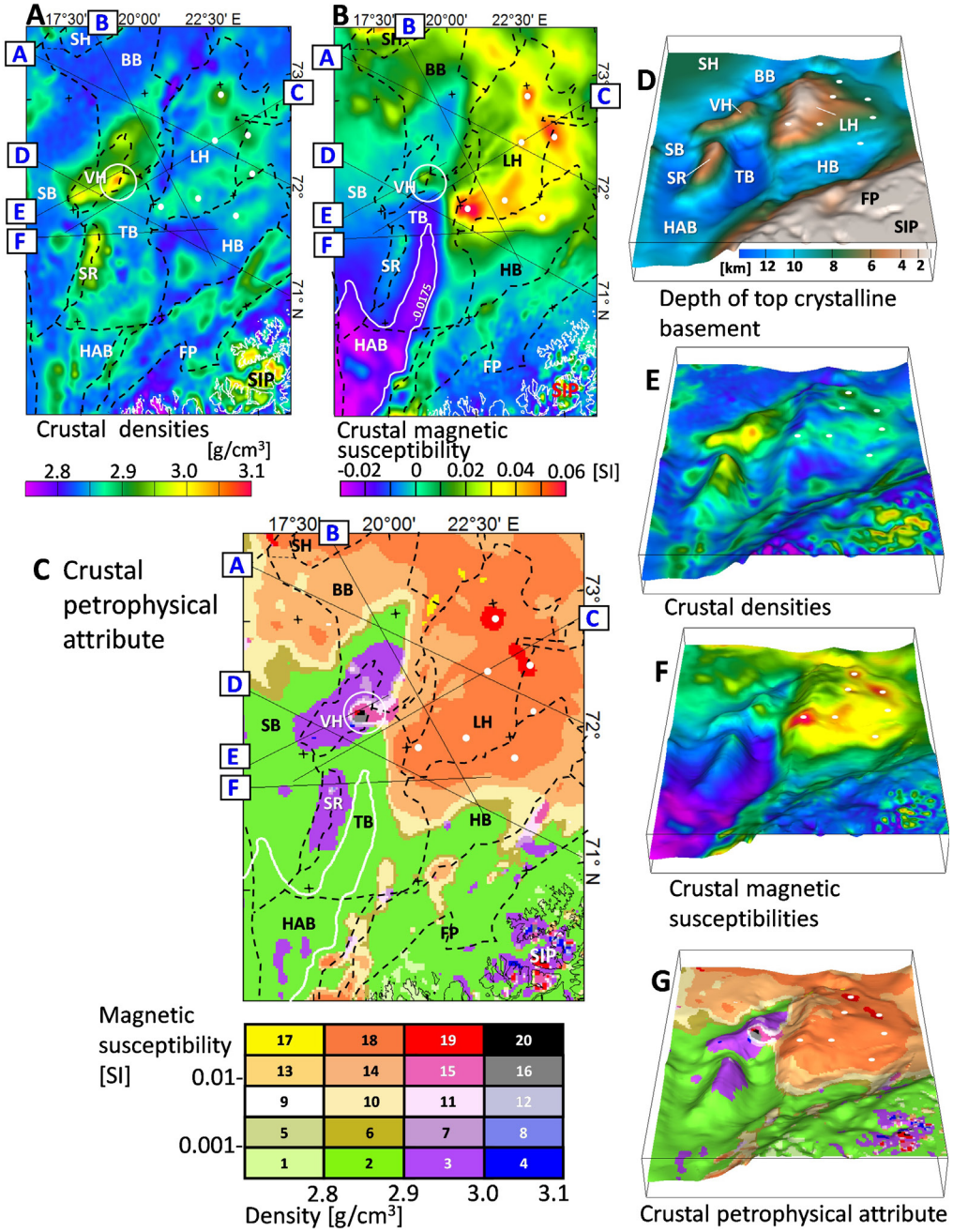

Figure 12. (A) Final model densities of the crystalline crust (crustal densities). (B) Final model magnetic susceptibilities of the crystalline crust (crustal magnetic susceptibilities) with contour at "-0.0175 SI" (white line). (C) (Crystalline) crustal petrophysical attribute with two-dimensional colour scale representing both densities and magnetic susceptibilities, colour table with colour identification code (ID), contour line (white) of susceptibility "-0.0175 SI", seismic profile locations (black lines with blue annotation; details in Fig. 1), boundaries of structural elements (black dashed, abbreviations in Fig. 2.). (D) 3D view of the topography of the top crystalline basement coated with (E) the crustal densities, with (F) the crustal magnetic susceptibilities, and with (G) the crustal petrophysical attribute. White dots and white ring mark interpreted intrusions that are discussed in the text.

centre and reflects the model structure used in this paper. Scenarios [b] and [c] yield the same gravity anomaly but by a different geometric structure. Model [b] represents a simple intrusion with one density (3.0 g/cm³), whereas model [c] represents an intrusion which has a high-density part (3.1 g/cm³) at greater depths. All three models have a central slab with a density of 3.0 g/cm³ (light grey) at the top crustal level. Consequently, if such scenarios occur, the largest value of the crustal density grid is a suitable estimate for the near-surface density of the intrusion. These considerations are also valid for the crustal magnetic susceptibilities.

As the magnetic susceptibility inversion does not account for NRM, this may lead to bias the case of high NRM in the crustal rocks. Some rock types may have high NRM as documented by ranges of Koenigsberger ratios for common rock types (Fig. 12B; Clark, 1997; Olesen et al., 2010; Henkel, 1991). Furthermore, mafic sills and dykes penetrating the shallow sedimentary strata may carry high NRMs and will as such also bias the crustal magnetic susceptibilities gained by the inversion.

Geological interpretation and discussion

The crustal petrophysical attribute map (Fig. 12C) is dominated by three colour groups indicating different characteristics in terms of combinations of densities and magnetic susceptibilities, and consequently, different rock types. (1) The first group, defined by warm colours with colour identification codes (ID) "14" and "18" indicating high magnetic susceptibilities and intermediate densities, covers 40% of the study area and includes mainly the area around the Loppa High and the northernmost parts of the Sørvestsnaget Basin and Bjørnøya Basin. (2) The second largest group comprises 38% of the study area and is represented by the green colour (ID "2"), which reflects low magnetic susceptibilities and intermediate densities and is representative of the basin areas, the Norwegian mainland outside the SIP, and the Finnmark platform. (3) The third group, defined by the purple colour (ID "3"), indicating high densities and low magnetic susceptibilities, accounts for 7% of the study area and includes mainly the Veslemøy High, Senja Ridge and Seiland Igneous Province (SIP). These regions are discussed in more detail below.

Norwegian mainland, Finnmark Platform, Hammerfest Basin, and eastern Tromsø Basin

Important constraints for the interpretation were found in the exposed onshore crustal rocks within and adjacent to the study area (Fig. 1). Averages of measured densities and magnetic susceptibilities of onshore rocks (Olesen et al., 2010) were displayed with the same colour scale as used for the crustal petrophysical attribute map and are referred to on the “onshore petrophysical attribute” map (Fig. 13C, for rock description and labels, see Table 3). On this map, the areas with metasedimentary rocks (labelled “[1]”,” [2]”, “[3]”) are displayed by light green colours (ID ”1”, “5”), whereas the crustal petrophysical attribute map (Fig. 13A) displays these areas by mainly bright green colour (ID “2”), indicating a higher density. Consequently, there must be rocks of higher densities at deeper crustal levels. Such rocks can be according to the mHPP (Fig. 11A) of intermediate–mafic intrusive or metamorphic character. The mafic–ultramafic rock parameters of the SIP (Table 3) appear in the onshore petrophysical attribute (Fig. 13C) with colour ID “8”, “12”, “16” and “20”, which indicates higher densities than in the crustal petrophysical attribute map (Fig. 13A) where they are dominated by purple colour (ID “3”). This suggests that the SIP, with its high-density mafic-ultramafic rocks, has a limited thickness and overlies rocks with lower crustal densities, consistent with crustal models of the SIP (Olesen et al., 1990; Pastore et al., 2016).

The coast-near part of the Finnmark Platform has the same colour in the crustal petrophysical attribute map (Fig. 13A) as the onshore parts of the KNC outside the SIP, which points towards similar crustal petrology. On the outer Finnmark Platform, a change towards higher densities occurs without an increase in magnetic susceptibilities as indicated by the sole occurrence of the bright green colour (ID "2") in the crustal petrophysical attribute map. This is shared with the entire southwestern part of the study area. Probable interpretations, according to the mHPP (Fig. 11A), are intermediate–mafic intrusive or metamorphic rocks, or metasedimentary rocks with their suggested distribution presented

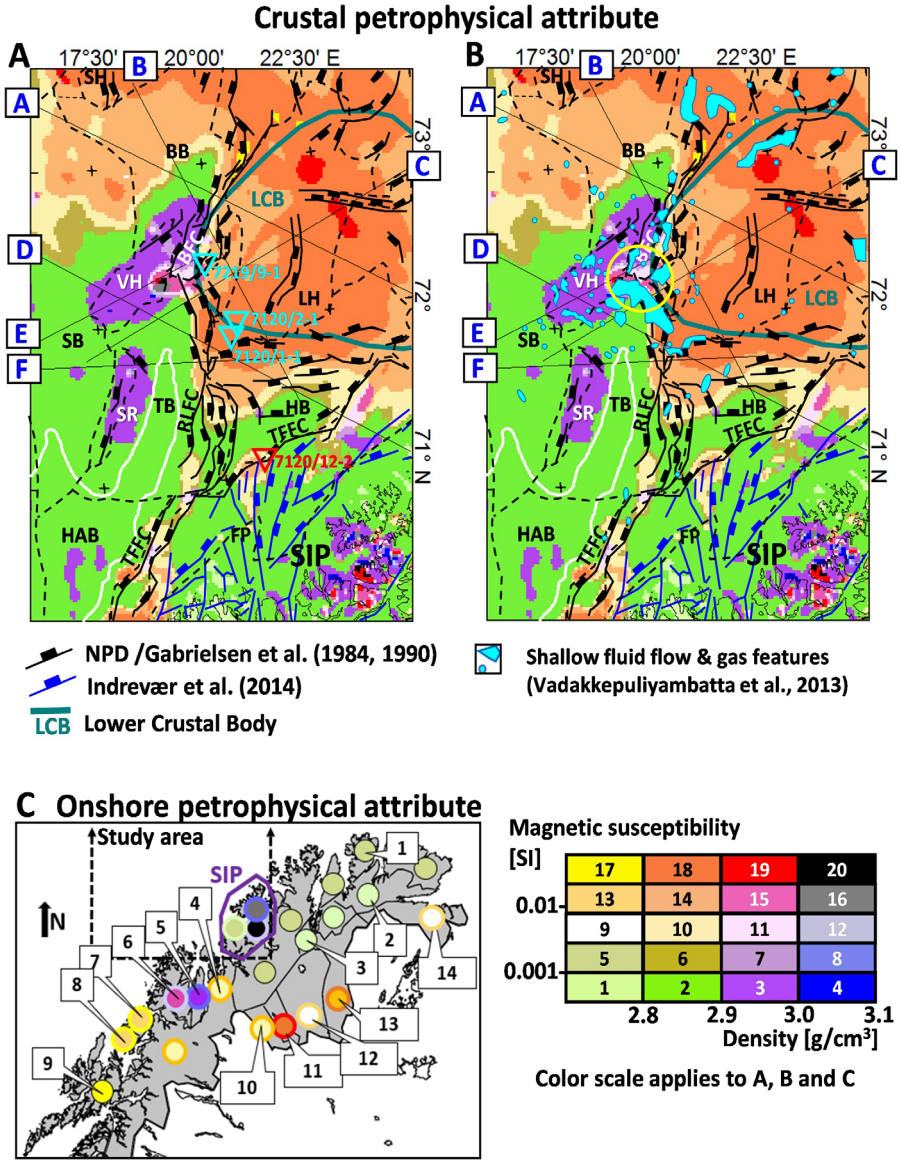

Figure 13. (A) Crustal petrophysical attribute with offshore faults (black lines; Norwegian Petroleum Directorate: www.factmaps.npd.no/factmaps/3_0/ visited 11.01.2022, based on Gabrielsen et al., 1984; 1990), near-shore and onshore faults (blue lines; Indrevær et al., 2014), and well locations penetrating the crystalline basement (red and blue triangles). (B) Crustal petrophysical attribute with areas of shallow fluid flow and gas features (Vadakkepuliyambatta et al., 2013), yellow ring marks area where methane flux may be linked with serpentinisation. BFC – Bjørnøyrenna Fault Complex, RLFC – Ringvassøy–Loppa Fault Complex, TFFC – Troms–Finnmark Fault Complex; boundaries of structural elements (black dashed, details in Fig. 1, abbreviations in Fig. 2), seismic profiles (black lines, details in Fig. 1), contour line (white) of crustal susceptibility "-0.0175 SI". (C) "Onshore petrophysical attribute" map presenting averages of densities and magnetic susceptibilities of onshore rocks (Olesen et al., 2010; Table 3): each circle indicates by its colour fill which petrophysical attribute is valid for the geographic area enclosed by black border lines or by coastline, a circle bounded by colour other than black indicates the range encompassed by the onshore petrophysical attributes of both colours.

in Fig. 14. Patches of brownish colours (ID "10", "14", "18"), indicating higher magnetic susceptibilities, are seen on the crustal petrophysical attribute map (Fig. 13A) along the Troms–Finnmark Fault Complex (TFFC) and the Ringvassøy Loppa Fault Complex (RLFC) as well as in the northern part of the Hammerfest Basin. The well 7120/12-2 penetrates the crystalline basement in one of these patches (see Fig. 13A). The well sample was described as quartz-rich mylonitic augen gneiss with a density of 2.666 g/cm^3 and magnetic susceptibility of 0.0002 SI (Table 3; Slagstad et al., 2008; Pascal et al., 2010). The measured density and magnetic susceptibility are lower than those indicated by the crustal petrophysical attribute map, suggesting that this site is underlain by rocks with higher crustal density

Table 3. Compilation of densities and magnetic susceptibilities of onshore rocks and offshore well cores. Geological survey of Norway: www.ngu.no/emne/kart-pa-nett "Berggrunn 1:250,000 vektor (Gammel)" visited 11.01.2022). M–arithmetic mean value, MD–median value, Q–Koenigsberger ratio; "A."–Archaean, FP–Finnmark Platform, GMC–Granite-Mangerite-Charnockite, LH–Loppa High, "P."–Proterozoic, TIB–Transscandinavian Igneous Belt; UM.A.–Uppermost Allochthon, U.A.–Upper Allochthon, M.A.–Middle Allochthon, L.A.–Lower Allochthon.

Geological Province	Rock type	Density [g/cm3]	Magnetic susceptibility [SI]	Koenigs-berger ratio	Reference
LH: 7120/2-1	1 Diabase (sample 1)	2.727	0.0340	0.20	Slagstad
	2 Diabase (sample 2)	2.762	0.0423	0.26	et al.
LH: 7120/1-1	3 Foliated amphibolite	3.085	0.0008	0.81	(2008) with
FP: 7120/12-2	4 Qtz-rich augen gneiss	2.666	0.0002	0.97	Q calculated
	Numbers correspond to Fig. 11				from NRM
Seiland	1 Gabbro (M)	3.053	0.0251	2.80	Pastore
Igneous	2 Gabbro (MD)	3.046	0.0072	0.90	et al.
Province	3 Ultramafic (M)	3.215	0.0106	4.20	(2018)
	4 Ultramafic (MD)	3.222	0.0053	1.60	
	5 Metasedimentary (M)	2.778	0.0025	1.60	
	6 Metasedimentary (MD)	2.761	0.0003	1.00	
	Numbers correspond to Fig. 11				
Onshore	1.(Meta-)Sedimentary (M.A.)	2.7-2.75	0.001-0.003		Densities
Norway	2.Metasedimentary (L.A.)	2.65-2.7	0.0001-0.0003		and suscep-
	3.Metasedimentary (L.A.)	2.65-2.7	<0.0001		tibilities:
	4.Mica schist, phyllite (U.A.)	2.8-2.85	0.003-0.01		Olesen
	5. Gabbro, amphibolite (UM.A.)	>2.95	0.0003-0.001		et al.
	6. Gabbro, amphibolite (UM.A.)	>2.95	0.003-0.01		(2010)
	7. GMC (P.)	2.7-2.75	0.01-0.03		
	8. GMC (P.)	2.65-2.7	0.01-0.03		Rock types:
	9. GMC, gneiss (TIB; P.)	2.75-2.8	>0.03		Geological
	10. Gneiss (A.)	2.7-2.75	0.01-0.03		Survey
	11. Greenstone (belt; P.)	2.85-2.95	>0.03		of Norway
	12. Gneiss (A.)	2.7-2.75	0.003-0.01		(see
	13. Greenstone (belt; P.)	2.8-2.85	0.01-0.03		caption)
	14. Gneiss (P.)	2.75-2.8	0.003-0.01		
	Numbers correspond to Fig.13C				

and higher magnetic susceptibilities. Zircon age dating resulted in 2750–2800 Ma which, together with the mineral composition, was interpreted by Pascal et al. (2010) to support a correlation with the Archaean rocks of Ringvassøya and Vanna (for location see label "[6]", Fig. 13C) in an NNE-ward continuation of the Precambrian basement present in Lofoten/Vesteralen and on the Troms islands. However, similar densities and magnetic susceptibilities were also reported for the Proterozoic Granite-Mangerite-Charnockite suites as well as for the Transscandinavian Igneous Belt as seen on the onshore petrophysical attribute map (Fig. 13C, Table 3) at the locations marked with labels "[7]", " [8]" and "[9]".

Loppa High

High-magnetic susceptibilities and intermediate densities visible as a wide belt on the crustal petrophysical attribute map (Fig. 12C, brownish colours, ID "14", "18") extend beyond the boundaries of the Loppa High (LH) into the platform areas in the east and the surrounding basins in the south

and west. In the northwest, this belt continues through the northwestern Bjørnøya Basin into the Stappen High (SH) indicating that the SH rocks may belong to the same rock province as the LH rocks. This hypothesis is supported by the previous work of Gernigon & Brønner (2012) who subdivided the area into nappe fragments based on magnetic and seismic data and reconstructed the nappe location to the time prior to backthrusting during the Caledonian mountain collapse. Their conclusion was that Late Palaeozoic rifting separated the SH from the LH. This hypothesis was supported by Shulgin et al. (2020) who applied an analysis combining seismic and gravity data. Furthermore, Lundin & Doré (2011) proposed that the Bjørnøya Basin is the northernmost tip of an Early Cretaceous rift system that spanned from the Rockall Trough in the south to the Bjørnøya Basin in the north and further separated the SH from the LH.

The crustal densities (Fig. 12A) of the LH show wide areas with a density range of 2.8–2.85 g/cm^3 which form the background for locally elevated positive densities. To derive the upper crustal background densities, the data needed to be corrected for a lower crustal body (LCB) known from seismic interpretation (profile A, Fig. 10A; Clark et al., 2013; profile C, Fig 10C; Aarseth, 2018). The lateral extension of the LCB as outlined by Clark et al. (2013) and Shulgin et al. (2020), is shown in Fig. 13A. Its density was estimated to 2.95 g/cm^3 by Gernigon et al. (2014), see profile B in Fig. 10B. In a 1D model scenario, assuming that the upper crust is twice as thick as the lower crust, an upper crustal background density range of 2.735–2.8 g/cm^3 was obtained. Alternatively, if the LCB fills the lower half of the crust, a density range of 2.65–2.75 g/cm^3 will be the result. These density range estimations were interpreted together with their high magnetic susceptibilities according to the mHPP to represent felsic to intermediate upper crustal rocks with their lateral extension shown in Fig. 14.

The largest crustal magnetic susceptibilities of the study area (0.04–0.06 SI, Fig. 12B) form a continuous belt with chains of oval to circular features along the southern and eastern part of the LH. The centres of these magnetic susceptibility highs (peaks) are marked by white dots which were transferred onto the crustal density map illustrating a clear correlation with elevated crustal densities (2.87–2.93 g/m^3, light to dark green colour, Fig. 12A). It was further investigated whether the peaks of the crustal magnetic susceptibility correlate with locations of local elevations in the top crystalline basement. For this purpose, the top basement depth (Fig. 12D) was coated with the crustal property grids as shown in Fig. 12E–G. The southwesternmost peak of the crustal magnetic susceptibility (Fig. 12F) is located near to a minor basement elevation, but otherwise, no correlation was found.

As explained in the chapter “Rock classifications method” and illustrated by Fig. 11C, a suitable density estimate for a simple intrusive body is the local maximum value of the crustal grid densities. A closer look at the density values at the white dots in Fig. 12A reveals a progressively increasing density from the southwestern corner of the LH towards the east and farther on towards north. The northernmost peaks reach densities of up to 2.93 g/cm^3 and meet, paired with a magnetic susceptibility of 0.05 SI, the category of mafic rock types according to the mHPP. In the southwestern corner of the LH, the density peak value of 2.87 g/cm^3 is paired with the highest magnetic susceptibility of the study area (0.06 SI; Fig. 12B) which indicates an intermediate–mafic intrusion according to the mHPP. Despite the differences in crustal parameters, it can be speculated whether the distribution of the interpreted intrusions in chains may point towards a common age and origin.

The geometry of one of the interpreted intrusions could be inferred from the northeastern part of profile C (Fig. 10C) which crosses through two of these magnetic susceptibility highs as seen in Fig. 12B. In profile view, these magnetic susceptibility highs frame a single zone of elevated densities, possibly the location of the root zone of an intrusion, overlain by widespread highly magnetic rocks at shallower depths. The total lateral extension of about 50 km indicates a major intrusion.

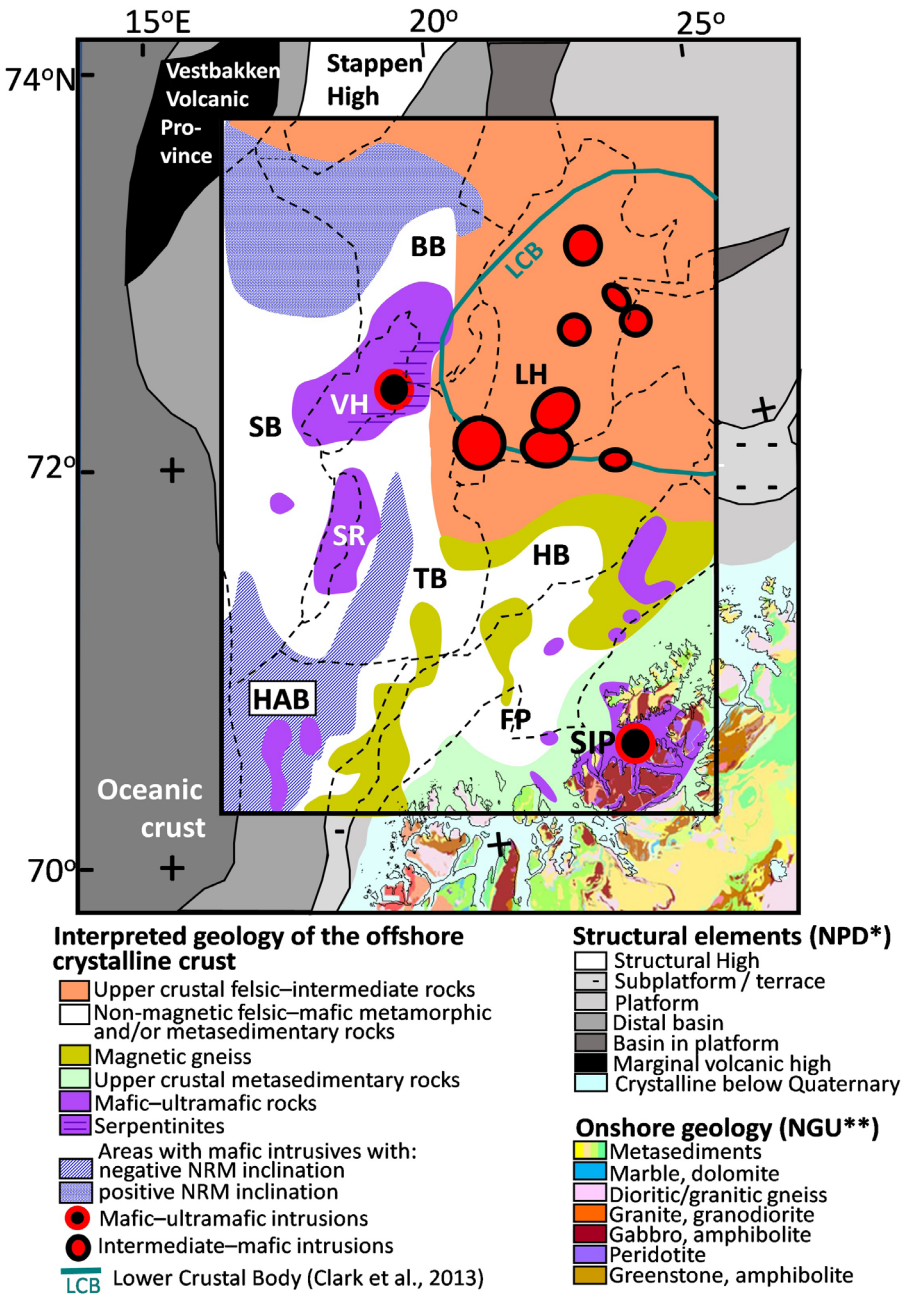

*Figure 14. Interpretation results of this study compiled in a new map showing the offshore geology of the crystalline crust. *Structural elements, and boundaries of structural elements at base Cretaceous level (black dashed; Norwegian Petroleum Directorate: www.factmaps.npd.no/factmaps/3_0/ visited 11.01.2022, based on Gabrielsen et al., 1984; 1990), abbreviations see Fig. 2). **Onshore geological map (Geological Survey of Norway: www.ngu.no/emne/kart-pa-nett "Berggrunn 1:250,000 vektor (Gammel)" visited 11.01.2022). NRM – Natural Remanent Magnetisation; BB – Bjørnøya Basin, FP – Finnmark Platform, HAB – Harstad Basin, HB –Hammerfest Basin, LH – Loppa High, SB – Sørvestsnaget Basin, SIP – Seiland Igneous Province, SR – Senja Ridge, TB – Tromsø Basin, VH – Veslemøy High.*

The top basement above the most magnetic intrusion in the southwestern corner of the LH was sampled by two wells (Fig. 13A, Table 3). Crustal metamorphic rocks of gneissic character were found in well 7120/1-1 (completion log: factpages.npd.no, visited 11.01.2022) and yield by analysis of a core fragment (described as "fine-grained, foliated amphibolite") a density of 3.085 g/cm^3, a magnetic susceptibility of 0.7771 10^{-3} SI and a Koenigsberger ratio of 0.81 (Olesen et al., 2007; Table 3). The completion log of well 7120/2-1 (factpages.npd.no, visited 11.01.2022) describes doleritic rocks. The analysis of two diabase samples revealed densities of 2.727 / 2.762 g/cm^3, magnetic susceptibilities of 0.034 / 0.042 SI and Koenigsberger ratios of 0.2 / 0.26 (Olesen et al.,

2007; Table 3). The Koenigsberger ratios of both wells are low indicating that NRM can be disregarded. The sampled amphibolites (7120/1-1) and doleritic dykes (7120/2-1) may be different expressions of the same mafic intrusion, that is suggested in this study. The average of the parameters from the wells suits the range of the inversion results, but also illustrates the inhomogeneity within the basement by the spread in the measured rock parameters. Completion log of well 7120/2-1 (factpages.npd.no, visited 11.01.2022) indicates that the doleritic rocks are embedded in the Carboniferous succession, suggesting a Carboniferous or younger age for the time of their emplacement. Support for a Carboniferous age was found in the Triassic sediments in the nearby Bjørnøya Basin from well 7219/9-1 (see Fig. 13A for location) which may have formed by erosion of the nearby LH rocks. One of the dominating zircon ages is Carboniferous (Fleming et al., 2016). It is noteworthy that a Carboniferous age was also found by dating of mafic dykes on Magerøya on the adjacent mainland (Lippard & Prestvik, 1997) located about 200 km to the southeast of the LH. The other dominant peak of the zircon ages from well 7219/9-1 points towards an Ediacaran age and is suggested to be sourced by the crustal rocks of the Veslemøy High as further discussed in the section "Veslemøy High, eastern Bjørnøya Basin, and Senja Ridge". A wide range of ages between 1000 and 1850 Ma is populated by the remaining zircon age peaks of minor size indicating a Proterozoic age, possibly related to the background rocks of the LH hosting the suggested Carboniferous intrusions, and/or to those of the Veslemøy High.

Western Bjørnøya Basin, Sørvestsnaget Basin, Harstad Basin and western Tromsø Basin

The western Bjørnøya Basin, Sørvestsnaget Basin, Harstad Basin and western Tromsø Basin have crustal densities between 2.8 and 2.85 g/cm^3 in a smooth pattern with minor areas of locally elevated densities of up to 2.9 g/cm^3 (Fig. 12A). These areas of elevated densities do not correspond to variations in crustal magnetic susceptibilities (Fig. 12B), or to top crystalline basement topography (Fig. 12D, E). Note that the uncertainty in crustal densities in deep basin areas, according to Scenario B in section "Uncertainty", is of the order of these small crustal density highs.

Moving southward, a remarkable pattern is observed in the westernmost basins by the crustal magnetic susceptibilities (Fig. 12B) with an almost steady decrease towards the south from zero at the latitude of the VH to negative values of up to -0.03 SI in the Harstad Basin. The western Tromsø Basin shows a similar trend and reaches highly negative crustal magnetic susceptibilities already farther north. Such amplitudes of negative magnetic susceptibilities are not found in common crustal rocks (cf., Clark, 1997) and need to be investigated. The error from the calculation of the crustal magnetic susceptibilities for the deep basinal parts (± 0.0066 SI, Scenario B in Table 2) is by far smaller than these negative values. Next, a bias in the crustal magnetic susceptibility caused by the massive salt domes due to the diamagnetic mineral halite with a magnetic susceptibility of -0.00001 SI (Clark, 1997) is also too small to explain these values. A larger bias can be caused by an unresolved edge effect. Any crustal body with high magnetic susceptibilities embedded in a host rock with low magnetic susceptibilities will generate a negative edge anomaly at the latitude of our study area. The size of the edge effect is smaller for a deep-rooted body than for a shallow crustal body (cf., Hinze et al., 2013). Our model style (Fig. 3A) mimics a deep-rooted body. Therefore, a hypothetical shallow crustal body that is terminated near the RLFC or the TFFC (see Fig. 13A for location) would be expected to cause negative magnetic anomalies in the Tromsø Basin. This would bias the crustal magnetic susceptibilities towards lower values. The highest edge effect would be expected in the northernmost Tromsø Basin adjacent to the very high magnetic anomaly in the southernmost Loppa High (Fig. 2B). Modelling tests with realistic magnetic attributes and geometries limited a possible edge effect to magnetic anomalies of at most -60 nT with a maximum lateral extent of about 25 km from the RLFC into the Tromsø basin. Such a scenario was calculated to result in a 0.006 SI decrease in crustal magnetic susceptibility.

Moving southward, along the eastern boundaries of the Tromsø Basin and the Harstad Basin, the magnetic anomaly in the graben shoulders is much lower (Fig. 2B), and consequently, the size of a hypothetical edge effect would also be correspondingly lower. On the contrary, it is observed that the crustal magnetic susceptibilities become even more negative towards the south. Consequently, even if the edge effect exists, it is not big enough to account for all the negative crustal magnetic susceptibilities. Therefore, the negative crustal magnetic susceptibilities were interpreted as an indication of NRM with a directional component that is opposite to the present-day geomagnetic field (International Geomagnetic Reference Field: https://www.ngdc.noaa.gov/IAGA/vmod/igrf.html). The area likely yielding a significant NRM is enclosed by a white contour line with a magnetic susceptibility of -0.0175 SI (Fig. 12B). This value was conservatively chosen to include the calculation error (Table 2), the unresolved edge effect and the error due to unknown geometries of the crustal magnetic source bodies deviating from our simple model structure. The area affected by negative NRM includes most of the Harstad Basin, a major part of the western Tromsø Basin and the southernmost Sørvestsnaget Basin. A possible explanation could be high abundance of sills, dykes and basalts in the sediments. While their very high NRM (see Koenigsberger ratios in Fig. 11B) would lead to a bias on the inverted crustal magnetic susceptibilities, their small rock volumes will only add minor deviations to the crustal density estimates. Consequently, the inverted crustal densities (Fig. 12A) should be the key for the interpretation of the crustal petrology. The crustal densities encountered on the westernmost Finnmark Platform and in the Hammerfest Basin are similar to those of the northern Bjørnøya Basin, Sørvestsnaget Basin, Harstad Basin and Tromsø Basin. Their crust is therefore suggested to consist of felsic–mafic metamorphic rocks or metasedimentary rocks having low magnetic susceptibilities. In this scenario, mafic sills, dykes and basalts in sediments and crust will likely be the main carrier of the magnetisation with a NRM direction opposite to the present-day geomagnetic field direction.

Sills, dykes and basalts are also encountered farther north in the northwestern part of the Sørvestsnaget and Bjørnøya basins as known from seismic interpretation for mafic intrusives and/or volcanics (Clark et al., 2013). However, this area shows elevated positive crustal magnetic susceptibilities indicating that the sills, dykes and basalts in this area have a NRM direction aligned with the present-day geomagnetic field direction. A possible explanation for the change in direction of the NRM could be that the sills, dykes, and basalts were intruded and cooled below the Curie temperature at times of different geomagnetic field directions. The gradual change in the magnetic susceptibilities from north to south within the westernmost basins may reflect a gradual change in the NRM directions. One possible explanation could be that the emplacement progression of the sills, dykes and basalts occurred during a geomagnetic field reversal (cf., Cox, 1968).

An alternative source for the varying NRM directions could be large crustal mafic intrusions, which are also known for high NRM (see Koenigsberger ratios for gabbro in Fig. 11B). An argument against this scenario is the rather smooth pattern of the crustal densities in Fig. 12A, which does not show any correlation with the pattern of the crustal magnetic susceptibilities in Fig. 12B. However, this observation may be questionable as the error in the crustal densities in the deep basin areas (Scenario B in Table 2: 0.034 g/cm^3) is relatively high and may hide a possible correlation. Also, the western Tromsø Basin is affected by negative crustal magnetic susceptibilities (Fig. 12B). With its exceptional low crustal thickness of less than 10 km, visible on seismic profile F (Figs. 9F & 10F; Breivik et al., 1999; Faleide et al., 2008), and the interpreted oblique rifting by Kairanov et al. (2021), mafic intrusions may have developed in crustal weakness zones along the axis of the basin. However, these hypotheses require further maturation, and an integrated seismic, gravity and magnetic interpretation could be a possible way forward.

The rock types suggested for the crust of the western Bjørnøya Basin, Sørvestsnaget Basin, Harstad Basin and western Tromsø Basin are included in the map shown in Fig. 14.

Veslemøy High, eastern Bjørnøya Basin and Senja Ridge

Large areas with high crustal densities combined with low magnetic susceptibilities shown in purple colour (ID “3”) on the crustal petrophysical attribute map (Fig. 12C) were found for the Veslemøy High (VH) and the Senja Ridge (SR). Along the eastern boundary of the VH and in the northern SR, the highest crustal densities form circular to elongated shapes (yellow to red colour; Fig. 12A). Notably, the highest density (red colour, Fig. 12A) in the offshore part of the entire study area occurs with a circular shape on the eastern VH. This location, marked by a white ring in Fig. 12A–C, is visible on the crustal petrophysical attribute map (Fig. 12C) by the colour “black” (ID “20”) in the centre, surrounded by pinkish colours (ID “15”, “11”). This shows that this density high is paired with elevated magnetic susceptibilities. Its marginal zone is crossed by seismic profile E (Fig. 10E) which documents a coincidence between these exceptionally high crustal densities and elevated seismic p-wave velocities located in the upper crust interpreted as intrusive rocks by Mjelde et al. (2002). Since these intrusive rocks do not fill the entire crust, their densities must be higher than in the crustal density grid (Fig. 12A) and thus give a clear indication for mafic-ultramafic rocks according to the mHPP. Another crustal density high in the western part of profile E (Fig. 10E) occurs at the location of bodies with high seismic velocities distributed at different levels throughout the crust. This location does not exhibit elevated magnetic susceptibilities. The highest p-wave velocity was found here in the lower crust with a value of 7.9 km/s (Mjelde et al., 2002) which coincides with the value of a peridotite (cf., Dentith & Mudge, 2014).

An interesting observation is that the VR and SR with their colour and patterns of the crustal petrophysical attribute map (Fig. 12C) express a great similarity with the Seiland Igneous Province (SIP). The SIP consists of a large volume of mafic and ultramafic rocks intruded into the metamorphosed metasedimentary rocks of the KNC (see section “Geological setting”). The SIP is emplaced in the upper crust, widely exposed at the surface and exhibits an average thickness of 2.5 km with deep reaching root zones down to a depth of 10 km or more (Pastore et al., 2016). This limited vertical extension explains the difference between average values of the SIP’s densities and magnetic susceptibilities from rock samples and the inverted crustal parameters as already discussed in the section “Norwegian mainland, Finnmark Platform, Hammerfest Basin and eastern Tromsø Basin”. The geometries and petrology with mafic and ultramafic intrusions forming the SIP may therefore be similar to those of the VH. Furthermore, a strong argument for a common origin was found in a well located near to the eastern boundary of the VH. Well 7219/9-1 (see Fig. 13A for location) penetrates Triassic sediments that may contain erosional products from the VH rocks. Detrital zircon age dating of these sediments by Fleming et al. (2016) showed a distinct peak at 585 Ma with a spread from 550 to 600 Ma. This includes the age of the SIP (580–560 Ma; Roberts et al., 2010). Larsen et al. (2018) suggested that the SIP is part of the "Central Iapetus Magmatic Province (CIMP)," and thus this large magmatic province may gain additional members with the VH and maybe also the SR.

However, for completeness of this discussion, alternative geological settings with mafic–ultramafic rocks need to be considered. Ophiolites (Dilek & Furnes, 2014), originating from crust and uppermost mantle of the Iapetus Ocean and its island arcs, are known to be part of the upper and the uppermost allochthons of the Scandinavian Caledonides (cf., Slagstad et al., 2014). Comparison of crustal densities and crustal magnetic susceptibilities of the VH and SR with those of the well explored Leka Ophiolite Complex (LOC) offshore central Norway shows similarities (Michels et al., 2018). However, an argument against an ophiolitic origin is the high crustal thickness of up to 20 km of the intrusive complex at the VH in the western part of profile E (Fig. 10E; Mjelde et al., 2002), exceeding both global values of common oceanic crustal thicknesses of 10–15 km (cf., Mooney et al., 1998) as well as being far higher than the thickness of the LOC estimated to 4 km in the most recent model by Michels et al. (2018).

Finally, mantle rocks can also be incorporated into the crust by exhumation as the result of ultraslow rifting with crustal hyperextension (e.g., Péron-Pindivic & Manatschal, 2009; Lundin & Doré, 2011) or by backsliding of a subducted slab (e.g., Spengler et al., 2009; Fichler et al., 2011). The exhumed mantle of both processes will be adjacent to and aligned with a deep reaching fault zone. The Bjørnøyrenna Fault Complex (BFC; see Fig. 13A for location) is a deep-reaching fault zone that was suggested by Ritzmann & Faleide (2007) to be a relic of the Iapetus Suture or, by Barrère et al. (2009), to be a major Caledonian weakness zone. Both publications showed in their models that rocks with high density and high seismic p-wave velocity are found along the BFC. This coincides with the findings of this study as documented on profiles A, B and C (Fig. 10) with elevated densities along the eastern flank of the Bjørnøya Basin. This area adjoins the VH to the north, as indicated by the location of the purple area (ID “3”) on the crustal petrophysical attribute map (Fig. 12C, G). However, the alignment of this area with the BFC is terminated in the centre of the VH, where the VH turns towards southwest and away from the large fault complexes of the BFC and RLFC. Farther south, the highest crustal densities forming the SR are also not adjacent to the deep reaching RLFC (Fig. 13A) but located along the western boundary of the Tromsø Basin. Consequently, the model of mantle exhumation may explain the high crustal densities in the Bjørnøya Basin, but it is not easily applicable for the southern part of the VH and the SR. These parts may therefore rather share their origin with the SIP as discussed above.

It is a noteworthy observation that areas of major gas and fluid flow in the upper sedimentary strata and on the seabed (Vadakkepuliyambatta et al., 2013) occur above and directly adjacent to the interpreted mafic–ultramafic rocks enclosing the VH and the westernmost part of the Bjørnøya Basin as shown in Fig.13B. The character of the gas of the observed shallow gas and fluid flow (Vadakkepuliyambatta et al., 2013) was investigated by chemical modelling of seismically mapped gas hydrates, which resulted in a composition consisting of methane and few percentages of higher order hydrocarbon gases and/or CO_2 (Chand et al., 2012). These authors suggested that the gases are a surface expression of the hydrocarbon system that is associated with a cluster of hydrocarbon discoveries, with the "Johan Castberg" hydrocarbon field on the western Loppa High as the most famous member (factmaps.npd.no/factmaps/3_0/ visited 11.01.2022). However, the spatial correlation between gas and fluid flow, and ultramafic rocks (Fig. 13B) may point towards a further source of methane related to serpentinisation. Serpentinisation is the hydration of peridotite, a reaction that is most effective at temperatures from 100 up to 370° C (Wegner & Ernst, 1983). This temperature range is certainly met in the crystalline crust of the VH and eastern Bjørnøya Basin according to the thermal models of Brönner et al. (2010). The process of serpentinisation of iron-bearing peridotites produces magnetite and hydrogen (cf., Evans et al., 2013). The latter is easily oxidised to methane and thus forms a common gas in areas of ongoing serpentinisation (cf., McCollom & Seewald, 2013). The magnetite produced by the serpentinisation would add to magnetic anomalies. Furthermore, volume increase of peridotite during serpentinisation (cf., Evans et al., 2013) will generate fractures that may work as migration pathways for the potential methane upward into the shallow sedimentary subsurface. It was further noted that elevated crustal magnetic susceptibilities occur below the greatest accumulation of fluid and gas flow features with the approximate location marked by a yellow ring in Fig. 13B. This may likely be caused by magnetite that was generated by serpentinisation, but highly magnetic gabbros as found in the SIP (Pastore et al., 2018) are also possible or a combination of both.

Based on these observations, the hypothesis is launched that serpentinisation contributes with methane to the observed fluid and gas system in the overlying sedimentary strata. With this hypothesis, the distribution of the fluid and gas flow features can reversely provide an idea of where serpentinised peridotites would be expected to occur within the interpreted mafic-ultramafic complex as outlined in Fig. 14.

Conclusions

A comprehensive workflow was developed targeting petrology of the crystalline crust in the south-western Barents Sea, combining gravity and magnetic interpretation with seismic and geological information. This included the construction of a 3D model from seafloor to mantle in terms of densities and magnetic susceptibilities, and a novel approach to interpret the crustal petrology. The crustal rocks that are expected to exist in the different parts of the southwestern Barents Sea are compiled in Fig. 14.

- Local low-density anomalies were found in the sediments, some of which are correlated with known salt occurrences in the Tromsø Basin and southern Sørvestsnaget Basin, while others, in the Bjørnøya Basin and Sørvestsnaget Basin, may indicate previously unknown locations of salt.
- Revised maps of the top crystalline basement and Moho depths were built from seismic profiles and expanded into map plane utilising earlier published maps and iterative model building.
- Crustal densities and magnetic susceptibilities were determined by inversion of gravity and magnetic anomalies in the framework of a 3D model from sea surface to mantle.
- Rock classification was performed by comparing the resulting (crystalline) crustal densities and magnetic susceptibilities with published ranges of crustal rock parameters. The latter were linked with a two-dimensional colour scale dedicated to combine the mapped crustal densities and magnetic susceptibilities into single map, a novel "crustal petrophysical attribute" map that assisted in the classification of the rock types.
- The crust of the Senja Ridge and Veslemøy High is interpreted as consisting of mafic-ultramafic intrusions that, it is argued, belong to the same large igneous province as the Seiland Igneous Province.
- The interpreted crust of the eastern Bjørnøya Basin supports the results of earlier interpretations and is suggested to consist of ultramafic rocks formed by mantle exhumation or backsliding of a subducted slab along the Bjørnøyrenna Fault Complex.
- An unusually high gas and fluid flux known within the shallow sediments at the Veslemøy High and eastern Bjørnøya Basin may indicate a possible link to methane from serpentinisation of the ultramafic rocks.
- Upper crustal rocks of the Loppa High with a northwestern extension into the southernmost Stappen High are interpreted as felsic–intermediate rocks of possible Precambrian age.
- The Loppa High is suggested to be intruded by chains of intermediate-mafic intrusions, possibly of Carboniferous age.
- The crystalline crust of the Hammerfest Basin, Harstad Basin, Tromsø Basin, Sørvestsnaget Basin and Bjørnøya Basin is interpreted as largely felsic–mafic metamorphic and/or meta-sedimentary rocks.
- An observed gradual change in polarity from negative to positive magnetic anomalies from the Harstad Basin through the Sørvestsnaget Basin is attributed to a change in direction of the natural remanent magnetisation (NRM) of sills, dykes and basalts.
- Mafic crustal intrusions with a NRM direction opposite to the present-day geomagnetic field are proposed for the western Tromsø Basin in areas of highly thinned crust.

Acknowledgements. Odleiv Olesen is warmly thanked for valuable discussions and support. Gaud Pouliquen, Suzanne A. McEnroe and Rune Berg-Edland Larsen are sincerely thanked for discussions and interest in this work. Eric James Ryan and Terje Solbakk are greatly thanked for language corrections and comments on the manuscript. Erik Lundin and Jörg Ebbing are sincerely thanked for their careful and detailed reviews. GEOSOFT is thanked for granting free access to software GMSYS3D™.

References

Aarseth, I. 2018: *Crustal structure across the western Barents Sea from deep seismic and potential field data*. PhD thesis, University of Bergen, 133 pp.

Afonso, J.C., Fernandez, M., Ranalli, G., Griffin, W.L. & Conolly, J.A.D. 2008: Integrated geophysical-petrological modeling of the lithosphere and sublithospheric upper mantle: Methodology and applications. *Geochemistry, Geophysics, Geosystems 9,* 36 pp. https://doi.org/10.1029/2007GC001834

Artemieva, I.M., Thybo, H. & Kaban, M.K. 2006: Deep Europe today: geophysical synthesis of the upper mantle structure and lithospheric processes over 3.5 Ga. *In* Gee, D.G. & Stephenson, R.A. (eds.): *European Lithosphere Dynamics,* Geological Society, London, Memoirs 32, pp. 11–41. https://doi.org/10.1144/GSL.MEM.2006.032.01.02

Barrère, C., Ebbing, J. & Gernigon, L. 2009: Offshore prolongation of Caledonian structures and basement characterization in the western Barents Sea from geophysical modelling. *Tectonophysics 470,* 71–88. https://doi.org/10.1016/j.tecto.2008.07.012

Barrère, C., Ebbing, J. & Gernigon, L. 2011: 3-D density and magnetic crustal characterization of the southwestern Barents Shelf: implications for the offshore prolongation of the Norwegian Caledonides. *Geophysical Journal International 184*, 1147–1166. https://doi.org/10.1111/j.1365-246X.2010.04888.x

Bauer, C. & Fichler, C. 2002: Quaternary lithology and shallow gas from high resolution gravity and seismic data in the central North Sea. Petroleum Geoscience 8, 229–236. https://doi.org/10.1144/petgeo.8.3.229

Breivik, A.J., Faleide, J.I. & Gudlaugsson, S.T. 1998: Southwestern Barents Sea margin: Late Mesozoic sedimentary basins and crustal extension. *Tectonophysics 293*, 21–44. https://doi.org/10.1016/S0040-1951(98)00073-0

Breivik, A.J., Verhoef, J. & Faleide, J.I. 1999: Effect of thermal contrasts on gravity modeling at passive margins: Results from the western Barents Sea. *Journal of Geophysical Research-Solid Earth 104*, 15293–15311. https://doi.org/10.1029/1998JB900022

Brigham, E.O. & Morrow, R.E. 1967: The fast Fourier transform. *IEEE Spectrum 4*, 63–70. https://doi.org/10.1109/MSPEC.1967.5217220

Brönner, M., Gernigon, L., Pascal, Ch., Koziel, J. & Marello, L. 2010: Barents Sea aeromagnetic remapping 2009 – BASAR-09. Acquisition and processing report and preliminary interpretation of the SW Barents Sea. *Geological Survey of Norway (NGU) Report 2010.056,* 210 pp.

Chand, S., Thorsnes, T., Rise, L., Brunstad, H., Stoddart, D., Bøe, R., Lågstad, P. & Svolsbru, T. 2012: Multiple episodes of fluid flow in the SW Barents Sea (Loppa High) evidenced by gas flares, pockmarks and gas hydrate accumulation. *Earth and Planetary Science Letters 331-332,* 305–314. https://doi.org/10.1016/j.epsl.2012.03.021

Chroston, P.N., Brooks, M. & Sellevoll, M.A. 1976: A seismic refraction line across the Seiland Igneous Province, northern Norway. *Norwegian Journal of Geology 56*, 211–216.

Clark, D.A. 1997: Magnetic petrophysics and magnetic petrology: aids to geological interpretation of magnetic surveys. *AGSO Journal of Australian Geology & Geophysics 17,* 83–103.

Clark, S.A., Faleide, J.I., Hauser, J., Ritzmann, O., Mjelde, R., Ebbing, J., Thybo, H. & Flüh, E. 2013: Stochastic velocity inversion of seismic reflection/refraction traveltime data for rift structure of the southwest Barents Sea. *Tectonophysics 593,* 135–150. https://doi.org/10.1016/j.tecto.2013.02.033

Corfu, F., Roberts, R.J., Torsvik, T.H., Ashwal, L.D. & Ramsay, D.M. 2007: Perigondwanan elements in the Caledonian nappes of Finnmark, northern Norway: implications for the paleogeographical framework of the Scandinavian Caledonides. *American Journal of Science 307*, 434–458. https://doi.org/10.2475/02.2007.05

Corfu, F., Andersen, T.B. & Gasser, D. 2014: The Scandinavian Caledonides: main features, conceptual advances, and critical questions. *In* Corfu, F., Gasser, D. & Chew, D.M. (eds.): *New Perspectives on the Caledonides of Scandinavia and Related Areas*, Geological Society, London, Special Publications 390, pp. 9–43. https://doi.org/10.1144/SP390.25

Cox, A. 1968: Lengths of Geomagnetic Polarity Intervals. *Journal of Geophysical Research 73,* 3247–3260. https://doi.org/10.1029/JB073i010p03247

Daly, J.S., Balagansky, V.V., Timmerman, M.J. & Whitehouse, M.J. 2006: The Lapland-Kola orogen: Palaeoproterozoic collision and accretion of the northern Fennoscandian lithosphere. *Geological Society, London, Memoirs 32,* 579–598. https://doi.org/10.1144/GSL.MEM.2006.032.01.35

Dentith, M. & Mudge, S.T. 2014: *Geophysics for the Mineral Exploration Geoscientist.* Cambridge University Press, 438 pp.

Dilek, Y. & Furnes, H. 2014: Ophiolites and their origins. *Elements 10,* 93–100. https://doi.org/10.2113/gselements.10.2.93

Doré, A.G. 1991: The Structural Foundation and Evolution of Mesozoic Seaways between Europe and the Arctic. *Palaeogeography, Palaeoclimatology, Palaeoecology 87*, 441–492. https://doi.org/10.1016/0031-0182(91)90144-G

Doré, A.G., Dahlgren, T., Flowerdew, M.J., Forthun, T., Hansen, J.O., Henriksen, L.B., Kåsli, K., Rafaelsen, B., Ryseth, A.E., Rønning, K., Similox-Tohon, D., Stoupakova, A. & Thießen, O. 2021: South-Central Barents Sea Composite Tectono-Sedimentary Element. *In* Drachev, S.S., Brekke, H., Henriksen, E. & Moore, T. (eds.): *Sedimentary Successions of the Arctic Region and Their Hydrocarbon Prospectivity,* Geological Society, London, Memoirs 57. https://doi.org/10.1144/M57-2017-42

Ebbing, J., Braitenberg, C. & Wienecke, S. 2007: Insights into the lithospheric structure and tectonic setting of the Barents Sea Region from isostatic considerations. *Geophysical Journal International 171,* 1390–1403. https://doi.org/10.1111/j.1365-246X.2007.03602.x

Ebbing, J. & Olesen, O. 2010: New compilation of top basement and basement thickness for the Norwegian continental shelf reveals the segmentation of the passive margin system. *Geological Society, London, Petroleum Geology Conference series 7,* 885–897. https://doi.org/10.1144/0070885

Elvebakk, G., Hunt, D.W. & Stemmerik, L. 2002: From isolated buildups to buildup mosaics: 3D seismic sheds new light on upper Carboniferous–Permian fault-controlled carbonate buildups, Norwegian Barents Sea. *Sedimentary Geology 152*, 7–17. https://doi.org/10.1016/S0037-0738(02)00232-4.

Enkin, R.J., Hamilton, T.S. & Morris, W.A. 2020: The Henkel Petrophysical Plot: Mineralogy and Lithology from Physical Properties. *Geochemistry, Geophysics, Geosystems 21*, 26 pp. https://doi.org/10.1029/2019GC008818.

Escartin, J., Hirth, G. & Evans, B. 2001: Strength of slightly serpentinized peridotites: implications for the tectonics of oceanic lithosphere. *Geology 29,* 1023–1026. https://doi.org/10.1130/0091-7613(2001)029<1023:SOSSPI>2.0.CO;2

Evans, B.W., Hattori, K. & Baronnet, A. 2013: Serpentinite: what, why, where? *Elements 9,* 99–106. https://doi.org/10.2113/gselements.9.2.99.

Faleide, J.I., Vågnes, E. & Gudlaugsson, S.T. 1993: Late Mesozoic-Cenozoic evolution of the south-western Barents Sea in a regional rift-shear tectonic setting. *Marine and Petroleum Geology 10,* 186–214. https://doi.org/10.1016/0264-8172(93)90104-Z

Faleide, J.I., Tsikalas, F., Breivik, A.J., Mjelde, R., Ritzmann, O., Engen, O., Wilson, J. & Eldholm, O. 2008: Structure and evolution of the continental margin off Norway and the Barents Sea. *Episodes 31,* 82–91. https://doi.org/10.18814/epiiugs/2008/v31i1/012

Fernàndez, M., Afonso, J.C. & Ranalli, G. 2010: The deep lithospheric structure of the Namibian volcanic margin. *Tectonophysics 481*, 68–81. https://doi.org/10.1016/j.tecto.2009.02.036

Fichler, C., Odinsen, T., Rueslåtten, H., Olesen, O., Vindstad, J.E. & Wienecke, S. 2011: Crustal inhomogeneities in the Northern North Sea from potential field modeling: Inherited structure and serpentinites? *Tectonophysics 510*, 172–185. https://doi.org/10.1016/j.tecto.2011.06.026

Fleming, E.J., Flowerdew, M.J., Smyth, H.R., Scott, R.A., Morton, A.C., Omma, J.E., Frei, D. & Whitehouse, M.J. 2016: Provenance of Triassic sandstones on the southwest Barents Shelf and the implication for sediment dispersal patterns in northwest Pangaea. *Marine and Petroleum Geology 78,* 516-535. https://doi.org/10.1016/j.marpetgeo.2016.10.005

Fyhn, M.B.W. & Hopper, J.R. 2021: NE Greenland Composite Tectono-Sedimentary Element, northern Greenland Sea and Fram Strait. In Drachev, S.S., Brekke, H., Henriksen, E.& Moore, T. (eds.): *Sedimentary Successions of the Arctic Region and Their Hydrocarbon Prospectivity,* Geological Society, London, Memoirs, 57. https://doi.org/10.1144/M57-2017-12

Gabrielsen, R.H. 1984: Long-lived fault zones and their influence on the tectonic development of the southwestern Barents Sea. *Journal of the Geological Society 141*, 651-662. https://doi.org/10.1144/gsjgs.141.4.0651

Gabrielsen, R.H., Foerseth, R., Hamar, G. & Rønnevik, H. 1984: Norwegian Petroleum Directorate Nomenclature of the main structural features on the Norwegian Continental Shelf north of the 62nd parallel. *In* Spencer, A.M. (ed.): *Petroleum Geology of the North European Margin,* Springer Netherlands, pp. 41–60. https://doi.org/10.1007/978-94-009-5626-1_5

Gabrielsen, R.H., Færseth, R.B., Jensen, L.N., Kalheim, J.E. & Riis, F. 1990: Structural elements of the Norwegian continental shelf. Part I: The Barents Sea Region. *Norwegian Petroleum Directorate Bulletin 6,* 33 pp.

Gasser, D., Jerabek, P., Faber, C., Stünitz, H., Menegon, L., Corfu, F., Erambert, M. & Whitehouse, M.J. 2015: Behaviour of geochronometers and timing of metamorphic reactions during deformation at lower crustal conditions: phase equilibrium modelling and U–Pb dating of zircon, monazite, rutile and titanite from the Kalak Nappe Complex, northern Norway. *Journal of Metamorphic Geology 33*, 7 513–534. https://doi.org/10.1111/jmg.12131

George, M., Olakunle, O.K., Johansen, S.E. & Abrahamsen, P. 2017: Seismic interpretation and characterization of anhydrite caprocks in the Tromsø Basin, SW Barents Sea. *Marine Geology 390,* 36–50. https://doi.org/10.1016/j.margeo.2017.04.013

Gernigon, L. & Brönner, M. 2012: Late Palaeozoic architecture and evolution of the southwestern Barents Sea: insights from a new generation of aeromagnetic data. *Journal of the Geological Society 169,* London, 449–459. https://doi.org/10.1144/0016-76492011-131

Gernigon, L., Brönner, M., Roberts, D., Olesen, O., Nasuti, A. & Yamasaki, T. 2014: Crustal and basin evolution of the southwestern Barents Sea: From Caledonian orogeny to continental breakup. *Tectonics 33*, 347–373. https://doi.org/10.1002/2013TC003439

Giles, M.R. 1997: *Diagenesis: A Quantitative Perspective.* Springer Netherlands, 526 pp.

Gradmann, S., Ebbing, J. & Fullea, J. 2013: Integrated geophysical modelling of a lateral transition zone in the lithospheric mantle under Norway and Sweden. *Geophysical Journal International 194.* 1358–1373. https://doi.org/10.1093/gji/ggt213

Grant, F.S. 1985: Aeromagnetics, geology and ore environments, I. Magnetite in igneous, sedimentary and metamorphic rocks: an overview. *Geoexploration 23,* 303–333. https://doi.org/10.1016/0016-7142(85)90001-8

Gudlaugsson, S.T., Faleide, J.I., Johansen, S.E. & Breivik, A.J. 1998: Late Palaeozoic structural development of the South-western Barents Sea. *Marine and Petroleum Geology 15,* 73–102. https://doi.org/10.1016/S0264-8172(97)00048-2

Guggisberg, B., Kaminski, W. & Prodehl, C. 1991: Crustal structure of the Fennoscandian Shield: A travel time interpretation of the long-range FENNOLORA seismic refraction profile. *Tectonophysics 195*, 105–137. https://doi.org/10.1016/0040-1951(91)90208-A

Harland, W.B. & Gayer, R.A. 1972: The Arctic Caledonides and earlier oceans. *Geological Magazin 109,* 289–314. https://doi.org/10.1017/S0016756800037717

Henkel, H. 1991: Petrophysical properties (density and magnetization) of rocks from the northern part of the Baltic Shield. *Tectonophysics 192,* 1–19. https://doi.org/10.1016/0040-1951(91)90242-K

Henriksen E., Ryseth, A.E., Larssen, G.B., Heide, T., Rønning, K., Sollid, K. & Stoupakova, A.V. 2011: Tectonostratigraphy of the greater Barents Sea: implications for petroleum systems. *In* Spencer, A.M., Embry, A.F., Gautier, D.L., Stoupakova, A.V. & Sørensen, K. (eds.): *Arctic Petroleum Geology,* Geological Society, London, Memoirs 35, 163–195. https://doi.org/10.1144/M35.10

Herrevold, T., Gabrielsen, R.H. & Roberts, D. 2009: Structural geology of the southeastern part of the Trollfjord-Komagelva Fault Zone, Varanger Peninsula, Finnmark, North Norway. Norwegian Journal of Geology 89, 305-325. ISSN 029-196X.

Herzberg, C.T., Fyfe, W.S. & Karr, M.J. 1983: Density Constraints on the Formation of the Continental Moho and Crust. *Contributions to Mineralogy and Petrology 84*, 1–5. https://doi.org/10.1007/BF01132324

Hinze, W.J., von Frese, R.R.B. & Saad, A.H. 2013: *Gravity and magnetic exploration: Principles, practices, and applications*. Cambridge University Press, 512 pp.

Indrevær, K., Stunitz, H. & Bergh, S.G. 2014: On Palaeozoic-Mesozoic brittle normal faults along the SW Barents Sea margin: fault processes and implications for basement permeability and margin evolution. *Journal of the Geological Society 171,* 831–846. https://doi.org/10.1144/jgs2014-018

Indrevær, K., Gabrielsen, R.H. & Faleide, J.I. 2016: Early Cretaceous synrift uplift and tectonic inversion in the Loppa High area, southwestern Barents Sea, Norwegian shelf. *Journal of the Geological Society 174*, 242–254. https://doi.org/10.1144/jgs2016-066

Indrevær, K., Gac, S., Gabrielsen, R.H. & Faleide, J.I. 2017. Crustal-scale subsidence and uplift caused by metamorphic phase changes in the lower crust: a model for the evolution of the Loppa High area, SW Barents Sea from Late Palaeozoic to Present. *Journal of the Geological Society,* 175, 497. https://doi.org/10.1144/jgs2017-063

Kairanov, B., Escalona, A., Norton, I. & Abrahamson, P. 2021: Early Cretaceous evolution of the Tromsø Basin, SW Barents Sea, Norway. *Marine and Petroleum Geology 123,* 18pp. https://doi.org/10.1016/j.marpetgeo.2020.104714

Kirkland, C.L., Daly, J.S. & Whitehouse, M.J. 2006: Granitic magmatism of Grenvillian and late Neoproterozoic age in Finnmark, Arctic Norway – constraining pre-Scandian deformation in the Kalak Nappe Complex. *Precambrian Research 145,* 24-52.

Klitzke, P., Faleide, J.I., Scheck-Wenderoth, M. & Sippel, J. 2015: A lithosphere-scale structural model of the Barents Sea and Kara Sea region. *Solid Earth 6*, 153–172. https://doi.org/10.5194/se-6-153-2015

Klitzke, P., Sippel, J., Faleide, J.I. & Scheck-Wenderoth, M. 2016: A 3D gravity and thermal model for the Barents Sea and Kara Sea. *Tectonophysics 684,* 131–147. https://doi.org/10.1016/j.tecto.2016.04.033

Laberg, S.J., Andreassen, K. & Vorren, T.O. 2012: Late Cenozoic erosion of the high-latitude south-western Barents Sea shelf revisited. *The Geological Society of America Bulletin 124,* 77–88. https://doi.org/10.1130/B30340.1

Larsen, R.B., Grant, T., Sørensen, B.E., Tegner, C., McEnroe, S.A., Pastore, Z., Fichler, C., Nikolaisen, E., Grannes, K.R., Church, N., ter Maat, G.W. & Michels, A. 2018: Portrait of a giant deep-seated magmatic conduit system: The Seiland Igneous Province. *Lithos 296–299*, 600–622. https://doi.org/10.1016/j.lithos.2017.11.013

Lippard, S.J. & Prestvik, T. 1997: Carboniferous dolerite dykes on Magerøy: new age determination and tectonic significance. *Geological Journal of Norway 77*, 59–163.

Litinsky, V.A. 1989: Concept of effective density: Key to gravity depth determinations for sedimentary basins. *Geophysics 54,* 1474–1482. https://doi.org/10.1190/1.1442611

Lund, C.-E. 1987: Crustal structure along the northern 'Fennolora' Profile. *Precambrian Research 35,* 195–206. https://doi.org/10.1016/0301-9268(87)90054-4
Lundin, E.R. & Doré, A.T. 2011: Hyperextension, serpentinization, and weakening: A new paradigm for rifted margin compressional deformation. *Geology 39*, 347–350. https://doi.org/10.1130/G31499.1

Lundin, E.R., Doré, A.G., Naliboff, J. & Van Wijk, J. 2022: Utilization of continental transforms in break-up: observations, models, and a potential link to magmatism. *Geological Society, London, Special Publications, 524*. https://doi.org/10.1144/SP524-2021-119

Marello, L., Ebbing, J. & Gernigon, L. 2013: Basement inhomogeneities and crustal setting in the Barents Sea from a combined 3D gravity and magnetic model. *Geophysical Journal International 193*, 557–584. https://doi.org/10.1093/gji/ggt018

McCollom, T.M. & Seewald, J.S. 2013: Serpentinites, Hydrogen, and Life. *Elements 9,* 129–134. https://doi.org/10.2113/gselements.9.2.129

Michels, A.C., McEnroe, S.A. & Fichler, C. 2018: Geophysical expression of the Leka Ophiolite, Norway, modeled from integrated gravity, magnetic and petrophysical data. *Norwegian Journal of Geology 98*, 103–125. https://doi.org/10.17850/njg98-1-07

Mjelde, R., Breivik, A.J., Elstad, H., Ryseth, A.E., Skilbrei, J.R., Opsal, J.G., Shimamura, H., Murai, Y. & Nishimura, Y. 2002: Geological development of the Sørvestsnaget Basin, SW Barents Sea, from ocean bottom seismic, surface seismic and potential field data. *Norwegian Journal of Geology 82*, 183–202

Mooney, W.D., Laske, G. & Masters, T.G. 1998: Crust 5.1: a global crustal model at 5°x5°. *Journal of Geophysical Research 103,* 727–747. https://doi.org/10.1029/97JB02122

Mørk, M.B.E., McEnroe, S.A. & Olesen, O. 2002: Magnetic susceptibilities of Mesozoic and Cenozoic sediments off Mid Norway and the role of siderite: implications for interpretation of high-resolution aeromagnetic data. *Marine and Petroleum Geology 19*, 1115–1126.
https://doi.org/10.1016/S0264-8172(02)00115-0

Norwegian Petroleum Directorate 2014: *CO2 Storage Atlas of the Barents Sea*.
https://www.npd.no/globalassets/1-npd/publikasjoner/atlas-eng/co2-atlas-barents-sea.pdf. (accessed 11. January 2022).

Olesen, O., Roberts, D., Henkel, H., Lile O.B. & Torsvik, T.H. 1990: Aeromagnetic and gravimetric interpretation of regional structural features in the Caledonides of West Finnmark and North Troms, northern Norway. *Geological Survey of Norway (NGU) Bulletin 419,* 1-24.

Olesen, O., Balling, N., Barrère, C., Breiner, N., Davidsen, B., Ebbing, J., Elvebakk, H., Gernigon, L., Koziel, J., Lutro, O., Midttømme, K., Nordgulen, Ø., Olsen, L., Osmundsen, P.T., Pascal, C., Ramstad, R.K., Rønning, J.S., Skilbrei, J.R., Slagstad, T. & Wissing, B. 2007: KONTIKI Final Report, Continental Crust and Heat Generation In 3D. *Geological Survey of Norway Report No. 2007.042.* 438 pp.

Olesen, O., Brönner, M., Ebbing, J., Gellein, J., Gernigon, L., Koziel, J., Lauritsen, T., Myklebust, R., Pascal, C., Sand, M., Solheim, D. & Usov, S. 2010: New aeromagnetic and gravity compilations from Norway and adjacent areas: methods and applications. *Petroleum Geology Conference series 7,* 559–586. https://doi.org/10.1144/0070559

Parker, R.L. 1973: The rapid calculation of potential anomalies. *Geophysical Journal International 31,* 447–455. https://doi.org/10.1111/j.1365-246X.1973.tb06513.x

Pascal, C., Balling, N., Barrère, C., Davidsen, B., Ebbing, J., Elvebakk, H., Mesli, M., Roberts, D., Slagstad, T. & Willemoes-Wissing, B. 2010: HeatBar Final Report 2010, Basement Heat Generation and Heat Flow in the western Barents Sea - Importance for hydrocarbon systems. *Geological Survey of Norway (NGU) Report 2010.030,* 91 pp.

Pastore, Z., Fichler, C. & McEnroe, A.S. 2016: The deep crustal structure of the mafic-ultramafic Seiland Igneous Province of Norway from 3D gravity modelling and geological implications. *Geophysical Journal International 207,* 1653–1666. https://doi.org/10.1093/gji/ggw362

Pastore, Z., Fichler, C. & McEnroe, S.A. 2018: Magnetic anomalies of the mafic/ultramafic Seiland Igneous Province. *Norwegian Journal of Geology 98,* 79–101. https://doi.org/10.17850/njg98-1-06

Péron-Pindivic, G. & Manatschal, G. 2009: The final rifting evolution at deep magma-poor passive margins from Iberia-Newfoundland: A new point of view. *International Journal of Earth Sciences 98*, 1581–1597. https://doi.org/10.1007/s00531-008-0337-9

Rider, M.H. 1986: *The geological interpretation of well logs.* John Wiley and Sons, Inc., New York, 192 pp. ISBN 0-470-20281-5

Riis, F., Vollset, J. & Sand, M. 1986: Tectonic development of the western margin of the Barents Sea and adjacent areas. *In* Halbouty, M.T. (ed.): *Future Petroleum Provinces of the World*. American Association of Petroleum Geologists (AAPG) Memoir 40, pp. 661–675. https://doi.org/10.1306/M40454C31

Ritzmann, O. & Faleide, J.I. 2007: Caledonian basement of the western Barents Sea. *Tectonics 26*, 20 pp. https://doi.org/10.1029/2006TC002059

Ritzmann, O., Maercklin, N., Faleide, J.I., Bungum, H., Mooney, W.D. & Detweiler, S.T. 2007: A three-dimensional geophysical model of the crust in the Barents Sea region: model construction and basement characterization. *Geophysical Journal International 170*, 417–435. https://doi.org/10.1111/j.1365-246X.2007.03337.x

Roberts, D. & Gee, D.G. 1985: An introduction to the structure of the Scandinavian Caledonides. In Gee, D.G. & Sturt, B.A. (eds.): *The Caledonide Orogen – Scandinavia and Related Areas.* Wiley, Chichester, pp.55–68.

Roberts, D. & Siedlecka, A. 2002: Timanian orogenic deformation along the northeastern margin of Baltica, Northwest Russia and Northeast Norway, and Avalonian–Cadomian connections. *Tectonophysics 352,* 169–184. https://doi.org/10.1016/S0040-1951(02)00195-6

Roberts, R.J., Corfu, F., Torsvik, T.H., Hetherington, C.J. & Ashwal, L.D. 2010: Age of alkaline rocks in the Seiland Igneous Province, Northern Norway. *Journal of the Geological Society 167*, 71–81. https://doi.org/10.1144/0016-76492009-014

Rowan, M.G. & Lindsø, S. 2017: Salt Tectonics of the Norwegian Barents Sea and Northeast Greenland Shelf. *In* Soto, JI, Flinch, J. & Tari, G. (eds.): *Permo-Triassic Salt Provinces of Europe, North Africa, and the Atlantic Margins*. Elsevier, 265–286. https://doi.org/10.1016/B978-0-12-809417-4.00013-6

Ryseth, A.E., Similox-Tohon, D. & Thieβen, O. 2021. Tromsø–Bjørnøya Composite Tectono-Sedimentary Element, Barents Sea. *In* Drachev, S.S., Brekke, H., Henriksen, E. & Moore, T. (eds.): Sedimentary Successions of the Arctic Region and Their Hydrocarbon Prospectivity, Geological Society, London, Memoirs 57. https://doi.org/10.1144/M57-2018-19

Sandwell, D.T., Müller, R.D., Smith, W.H.F., Garcia, E. & Francis R. 2014: New global marine gravity model from CryoSat-2 and Jason-1 reveals buried tectonic structure. *Science 346,* 65–67. https://doi.org/10.1126/science.1258213

Sclater, J.G. & Christie, P.A.F. 1980: Continental stretching: An explanation of the mid-Cretaceous subsidence of the Central North Sea Basin. *Journal of Geophysical Research 85*, 3711–3739. https://doi.org/10.1029/JB085iB07p03711

Shulgin, A., Faleide, J.I., Mjelde, R., Breivik, A. & Huismans, R. 2020: Crustal domains in the Western Barents Sea. *Geophysical Journal International 221,* 2155–2169. https://doi.org/10.1093/gji/ggaa112

Siedlecka, A., Roberts, D., Nystuen, J.P. & Olovyanishnikov, V.G-. 2004: Northeastern and north-western margins of Baltica in Neoproterozoic time: evidence from the Timanian and Caledonian orogens. *Geological Society of London, Memoirs, 30,* 169-190.

Skilbrei, J.R. 1995: Aspects of the geology of the southwestern Barents Sea from aeromagnetic data. *Geological Survey of Norway (NGU) Bulletin 427,* 64–67.

Slagstad, T., Barrère, C., Davidsen, D. & Ramstad, R.K. 2008: Petrophysical and thermal properties of pre-Devonian basement rocks on the Norwegian continental margin. *Geological Survey of Norway (NGU) Bulletin 448,* 1–6.

Slagstad, T., Pin, C., Roberts, D., Kirkland, C.L., Grenne, T., Dunning, G., Sauer, S. & Andersen, T. 2014: Tectonomagmatic evolution of the Early Ordovician suprasubduction-zone ophiolites of the Trondheim Region, Mid-Norwegian Caledonides. *In* Corfu, F., Gasser, D. & Chew, D.M. (eds.): *New Perspectives on the Caledonides of Scandinavia and Related Areas*. Geological Society, London, Special Publications 390, pp. 541-561. https://doi.org/10.1144/SP390.25

Smelror, M., Petrov, O., Larssen, G.B. & Werner, S.C. 2009: ATLAS: *Geological history of the Barents Sea.* Geological Survey of Norway, Trondheim.

Smith, W.H.F. & Sandwell, D.T. 1997: Global seafloor topography from satellite altimetry and ship depth soundings. *Science 277*, 1957–1962. https://doi.org/10.1126/science.277.5334.1956

Spengler, S., Brueckner, H.K., van Roermund, H.L.M., Drury, M.R. & Mason, P.R.D. 2009: Long-lived, cold burial of Baltica to 200 km depth. *Earth and Planetary Science Letters 281*, 27–35. https://doi.org/10.1016/j.epsl.2009.02.001

Stadtler, C., Fichler, C., Hokstad, K., Myrlund, E.A., Wienecke, S. & Fotland, B. 2014: Improved salt imaging in a basin context by high resolution potential field data: Nordkapp Basin, Barents Sea. *Geophysical Prospecting 62*, 615–630. https://doi.org/10.1111/1365-2478.12101

Tsikalas, F. 1992: *A study of seismic velocity, density, and porosity in Barents Sea wells (N. Norway).* M.Sc Thesis, University of Oslo.

Tsikalas, F., Faleide, J.I., Eldholm, O. & Blaich, O.A. 2012: The NE Atlantic conjugate margins. *In* Roberts, D. G. (ed.): *Regional Geology and Tectonics: Phanerozoic Passive Margins, Cratonic Basins and Global Tectonic Maps,* Elsevier, 140–201. https://doi.org/10.1016/B978-0-444-56357-6.00004-4

Vadakkepuliyambatta, S., Bünz, S., Mienert, J. & Chand, S. 2013: Distribution of subsurface fluid-flow systems in the SW Barents Sea. *Marine and Petroleum Geology 43*, 208–221. https://doi.org/10.1016/j.marpetgeo.2013.02.007

Wegner, W.E. & Ernst, W.G. 1983: Experimentally determined hydration and dehydration reaction rates in the system MgO-SiO2-H2O. *American Journal of Science 283A*, 151–180.

Winter, J.D. 2010: *Principles of igneous and metamorphic petrology, 2nd edition*. Prentice Hall, 702 pp.

Zhao, X., Riisager, P., Antretter, M., Carlut, J., Lippert, P., Liu, Q., Galbrun, B., Hall, S., Delius, H. & Kanamatsu, T. 2006: Unraveling the magnetic carriers of igneous cores from the Atlantic, Pacific, and the southern Indian oceans with rock magnetic characterization. *Physics of the Earth and Planetary Interiors 156,* 294–328. https://doi.org/10.1016/j.pepi.2005.08.005